Supplementary Information

Itinerant and topological excitations in a honeycomb spiral spin liquid candidate

Yuqian Zhao, Xuping Yao, Xun Chen, Zongtang Wan, Zhaohua Ma, Xiaochen Hong & Yuesheng Li

Supplementary Note 1. Thermal conductivity and thermal Hall effect measurements

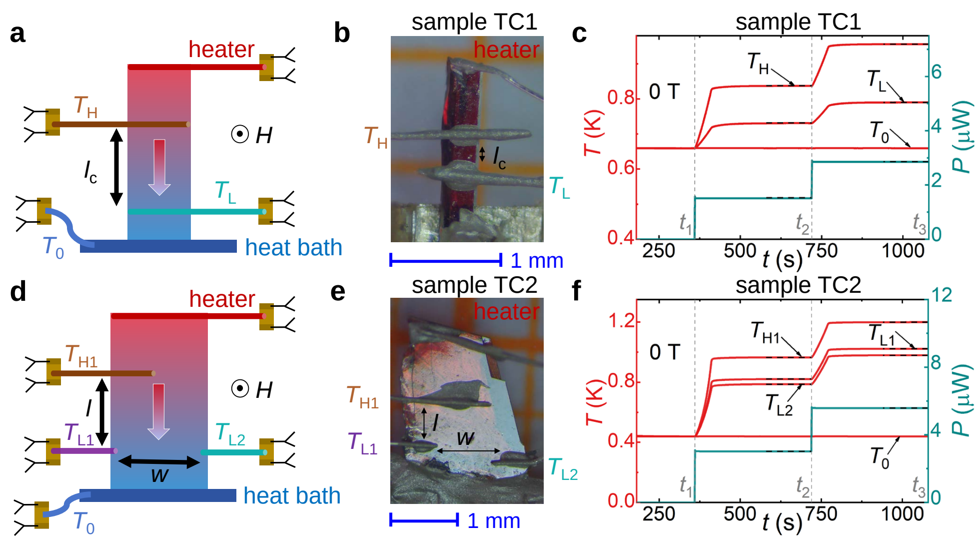

Supplementary Fig. 1 | Samples TC1 and TC2. a,**d**, Schematic diagrams of the thermal conductivity and thermal Hall effect measurement setups, respectively. **b**,**e**, Single-crystal samples TC1 and TC2 of GdZnPO used for the thermal conductivity and thermal Hall effect measurements. **c**,**f**, Temperature readings from thermometers and heater power measurements for samples TC1 and TC2 during the collection of two representative data points shown elsewhere. The dashed horizontal lines indicate the average values used to evaluate the longitudinal thermal conductivity and thermal Hall conductivity. Two different heating powers were applied at each temperature T_0 to test the reliability of our experimental setup (see text below).

We first conducted longitudinal thermal conductivity and thermal Hall conductivity measurements on four randomly selected GdZnPO crystals TC1-TC4, as shown in Supplementary Figs. 1 and 2. The back-scattering Laue x-ray diffraction (XRD; detector: LAUESYS_V_674, Photonic Science & Engineering Ltd) patterns from the upper surfaces of these samples displayed sharp reflections (see Supplementary Fig. 3), indicating high crystallization quality. The XRD results also confirmed that the longest crystal directions were along [110] in the ab plane, ensuring the heat current predominantly flowed along this direction, with the magnetic field applied along the c axis for all samples. The average cross-section areas of the heat flow (thickness $\times$ full width) were measured using a microscope: A = 0.17×0.29, 0.06×1.63, 0.06×0.83, and

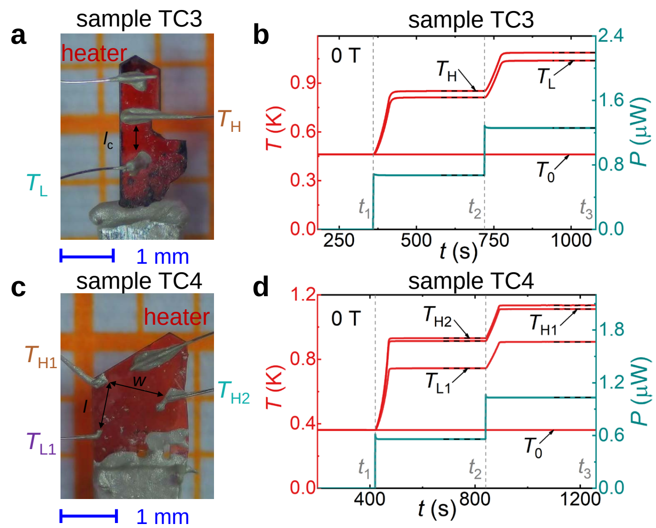

Supplementary Fig. 2 | Samples TC3 and TC4. a,**c**, Single-crystal samples TC3 and TC4 of GdZnPO used for thermal conductivity and thermal Hall effect measurements, respectively. **b**,**d**, Temperature readings from thermometers and heater power measurements for samples TC3 and TC4 during the collection of two representative data points shown elsewhere. The dashed horizontal lines indicate the average values used to evaluate the longitudinal thermal conductivity and thermal Hall conductivity. Two different heating powers were applied at each temperature T_0 to test the reliability of our experimental setup (see text below).

0.03×1.74 mm^2 for samples TC1-TC4, respectively. Silver wires to the thermometers and a chip resistance heater were attached to the sample surfaces with silver paint (Supplementary Figs. 1 and 2), guiding the heat flow approximately along [110]. The measured distances between the temperature sensors were as follows: between T_H and T_L along the heat flow, l_c = 0.18 mm (Supplementary Fig. 1b) and 0.49 mm (Supplementary Fig. 2a) for samples TC1 and TC3, respectively; between T_H1 and T_L1 along the heat current, l = 0.47 mm (Supplementary Fig. 1e) and 1.01 mm (Supplementary Fig. 2c) for samples TC2 and TC4, respectively. The distances perpendicular to the heat current were w = 1.05 mm between T_L2 and T_L1 for sample TC2 (Supplementary Fig. 1e), and 1.26 mm between T_H2 and T_H1 for sample TC4 (Supplementary Fig. 2c).

All RuO_2 chip thermometers (T_H, T_L, T_H1, T_L1, T_H2, and T_L2; RX-102A-BR, LakeShore) were *in situ* calibrated against a reference thermometer (T_0, RX-102B-RS-0.02B, LakeShore, calibrated down to 18 mK) prior to each measurement. Calibration was performed under the temperature range (0.03 to 2 K) and magnetic field conditions (-12 to 12 T), by turning off the heater power (P = 0) at $t < t_1$ (Supplementary Figs. 1c,f and 2b,d). To ensure a high signal-to-noise ratio, all thermometers were measured using Lakeshore Model 372 resistance bridges/temperature controllers equipped with specially designed internal

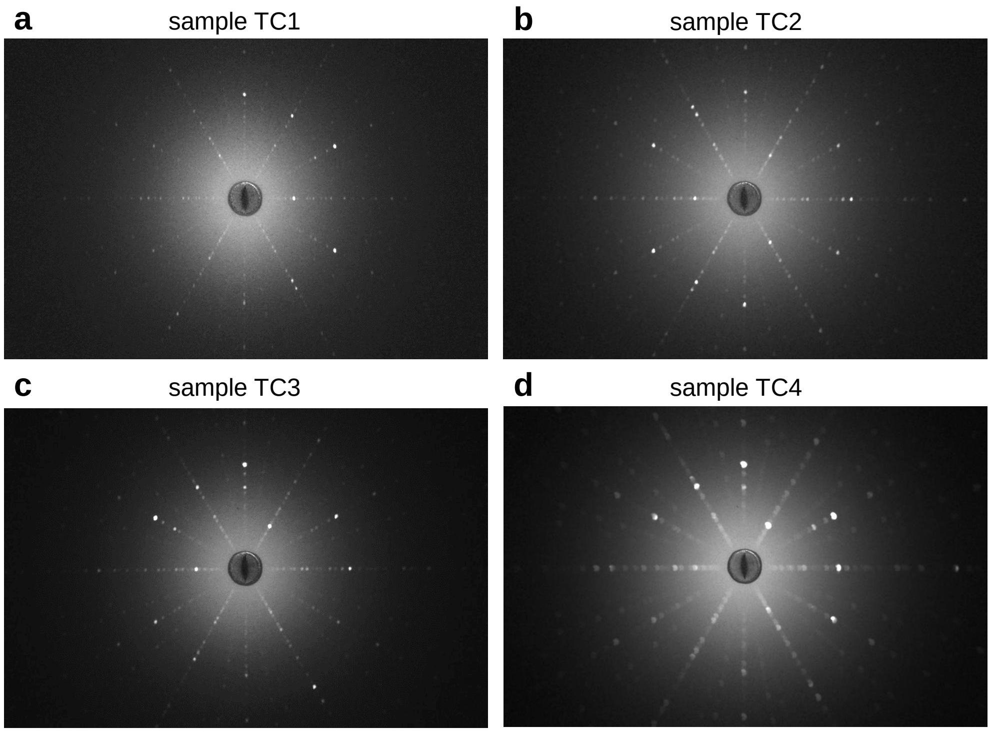

Supplementary Fig. 3 | Laue x-ray diffraction (XRD) patterns. a-d, Patterns measured on the upper surfaces of samples TC1-TC4 following thermal conductivity and thermal Hall effect measurements. All Laue XRD measurements were performed sequentially under identical conditions: tungsten target (20 kV, 15 mA), 400 s exposure, and a consistent sample-detector distance.

lock-in amplifiers. The longitudinal thermal conductivity (κ_{xx}) and thermal Hall conductivity (κ_{xy}) measurements were conducted using a standard four-wire steady-state method [1] for the elongated samples TC1 and TC3 (Supplementary Figs. 1c and 2b), and a five-wire steady-state method for the wider samples TC2 and TC4 (Supplementary Figs. 1f and 2d). Measurements were performed in high vacuum using a ^{3}He-^{4}He dilution refrigerator (KELMX-400, Oxford Instruments). The lower and higher power data were averaged over $(t_1 + t_2)/2 < t < t_2$ and $(t_2 + t_3)/2 < t < t_3$, respectively (Supplementary Figs. 1c,f and 2b,d), and are presented in Supplementary Figs. 4 and 5 as solid and open data points.

The longitudinal thermal resistivity and thermal Hall resistivity are defined as ω_{xx} = $A\nabla_x T/P$ and ω_{xy} = $A\nabla_y T/P$, respectively, where $\nabla_x T$ and $\nabla_y T$ denote the temperature gradients parallel and perpendicular to the heat flow. Typically, $|\nabla_y T|$ ($|\omega_{xy}|$) is significantly smaller than $\nabla_x T$ (ω_{xx}). Consequently, the longitudinal thermal conductivity is given by κ_{xx} = $\omega_{xx}/(\omega_{xx}^2 + \omega_{xy}^2) \approx P/(A\nabla_x T)$ and the thermal Hall conductivity by κ_{xy} = $\omega_{xy}/(\omega_{xx}^2 + \omega_{xy}^2)$ = $\kappa_{xx}\nabla_y T/\nabla_x T$. For the elongated samples TC1 and TC3, $\nabla_x T$ = $(T_{\rm H} - T_{\rm L})/l_{\rm c}$ and the sample temperature T = $(T_{\rm H} + T_{\rm L})$/2. For the wider crystals TC2 and TC4, T

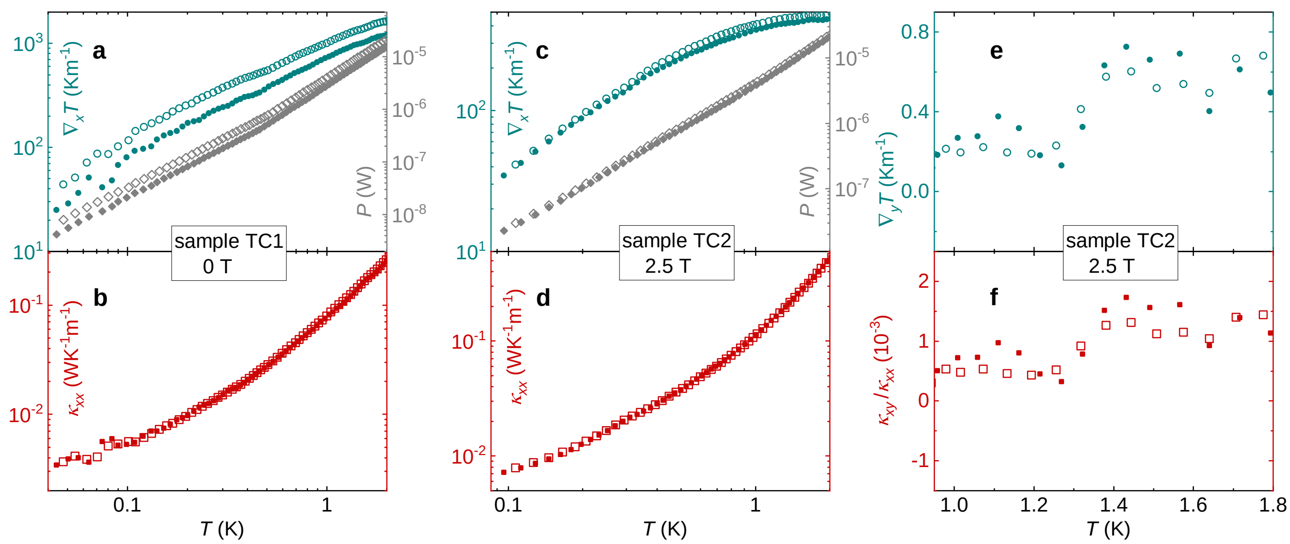

Supplementary Fig. 4 | Responses to heater power measured on samples TC1 and TC2. a, Heating power (P) applied to single-crystal sample TC1 and the resulting temperature gradient along the heat flow ($\nabla_x T$). **b**, Thermal conductivity of sample TC1, κ_{xx}. **c-f**, Raw thermal conductivity data measured at $\mu_0 H$ = 2.5 T on single-crystal sample TC2. The heating power P is shown in **c**, and the corresponding temperature gradients parallel and perpendicular to the heat flow, $\nabla_x T$ and $\nabla_y T$, are shown in **c** and **e**, respectively. κ_{xx} (**d**) and κ_{xy}/κ_{xx} ($\equiv$ $\nabla_y T/\nabla_x T$) (**f**) were measured on sample TC2. Solid and open symbols represent lower and higher power data, respectively.

= $(T_{\mathrm{H1}} + T_{\mathrm{L1}})/2$, and $\nabla_x T(H)$ was calculated as $[(T_{\mathrm{H1}} - T_{\mathrm{L1}})|_H + (T_{\mathrm{H1}} - T_{\mathrm{L1}})|_{-H}]/(2l)$ to eliminate transverse responses caused by contact misalignment (see Supplementary Figs. 1e and 2c), since $\nabla_x T$ is an even function of the applied magnetic field H. Similarly, we evaluated $\nabla_y T(H) = [(T_{\mathrm{L2}} - T_{\mathrm{L1}})|_H - (T_{\mathrm{L2}} - T_{\mathrm{L1}})|_{-H}]/(2w)$ and $[(T_{\mathrm{H2}} - T_{\mathrm{H1}})|_H - (T_{\mathrm{H2}} - T_{\mathrm{H1}})|_{-H}]/(2w)$ for samples TC2 and TC4, respectively, to eliminate longitudinal responses, given that $\nabla_y T$ is an odd function of H. For each sample and magnetic field, the measured κ_{xx} remained independent of the heater power P, indicating a good linear response and minimal heat leakage in our experimental setup (e.g., see Supplementary Figs. 4 and 5). Furthermore, the measured κ_{xy}/κ_{xx}, and thus κ_{xy}, also showed negligible dependence on P within a reasonable error range (see Supplementary Figs. 4 and 5).

For sample TC2, the measured longitudinal thermal conductivity $\kappa_{xx} = Pl/[A(T_{\mathrm{H1}} - T_{\mathrm{L1}})]$ remains independent of the magnetic field's sign within a reasonable error range, as shown in Supplementary Fig. 6c, confirming that both κ_{xx} and $\nabla_x T$ are even functions of H. Conversely, the transverse-to-longitudinal temperature gradient ratio, $(T_{\mathrm{L2}} - T_{\mathrm{L1}})/(w\nabla_x T)$, clearly depends on the sign of H (see Supplementary Fig. 6a), reflecting the odd-function nature of $\nabla_y T$ due to $\kappa_{xy} \neq 0$. While the crystal size of sample

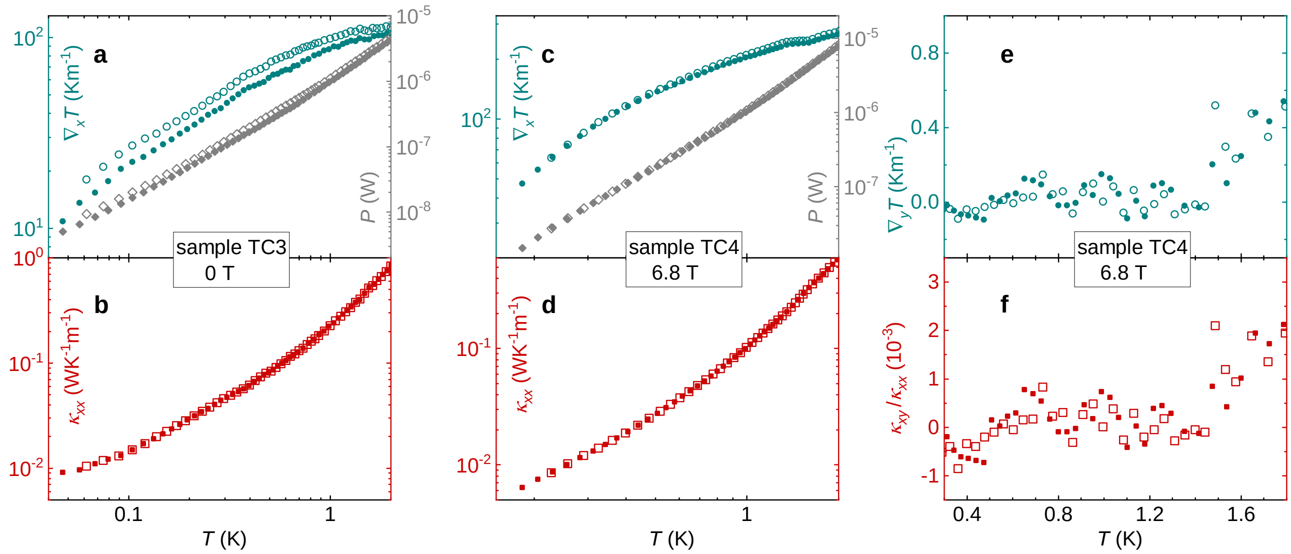

Supplementary Fig. 5 | Responses to heater power measured on samples TC3 and TC4. a, Heating power (P) applied to single-crystal sample TC3 and the resulting temperature gradient along the heat flow ($\nabla_x T$). **b**, Thermal conductivity of sample TC3, κ_{xx}. **c-f**, Raw thermal conductivity data measured at $\mu_0 H$ = 6.8 T on single-crystal sample TC4. The heating power P is shown in **c**, and the corresponding temperature gradients parallel and perpendicular to the heat flow, $\nabla_x T$ and $\nabla_y T$, are shown in (**c**) and (**e**), respectively. κ_{xx} (**d**) and κ_{xy}/κ_{xx} ($\equiv \nabla_y T/\nabla_x T$) (**f**) were measured on sample TC4. Solid and open symbols represent lower and higher power data, respectively.

TC4 is sufficient for thermal Hall conductivity measurements, its lower crystallization quality–evidenced by broader reflections in its Laue XRD pattern (see Supplementary Fig. 3)–distinguishes it from the other samples.

In insulators, crystal imperfections can introduce carriers, potentially reducing electrical resistivity [13]. The GdZnPO single crystals are good insulators with high resistivity, $\rho^{\mathrm{e}}_{xx} \geq 300$ Ωm, below 300 K (see Fig. 2 in the main text). Sample TC4 shows a significantly smaller electric gap (∼220 K) compared to the other samples (≥330 K), confirming its inferior crystallization quality. As the temperature drops below ∼0.3 K, κ_{xx}/T for sample TC4 shows a downturn with notably lower values, contrasting sharply with the other samples (see Fig. 2 in the main text). Additionally, the κ_{xy} signals from sample TC4 are noticeably noisier than those from sample TC2 (compare Supplementary Fig. 6d,e with Supplementary Fig. 6a,b).

From fitting κ_{xx} below 1 K, we obtained the phonon mean free paths, $\lambda_{\mathrm{p}} \sim 4.8$, 10.9, 14.5, and 13.8 μm for samples TC1-TC4, respectively—much smaller than the corresponding average sample width W = $2\sqrt{A/\pi}$ (∼251, 353, 252, and 258 μm), where A denotes the cross-sectional area (see Supplementary Table 1). This suggests that the crystallinity quality of the randomly selected samples TC1-TC4 may simply have

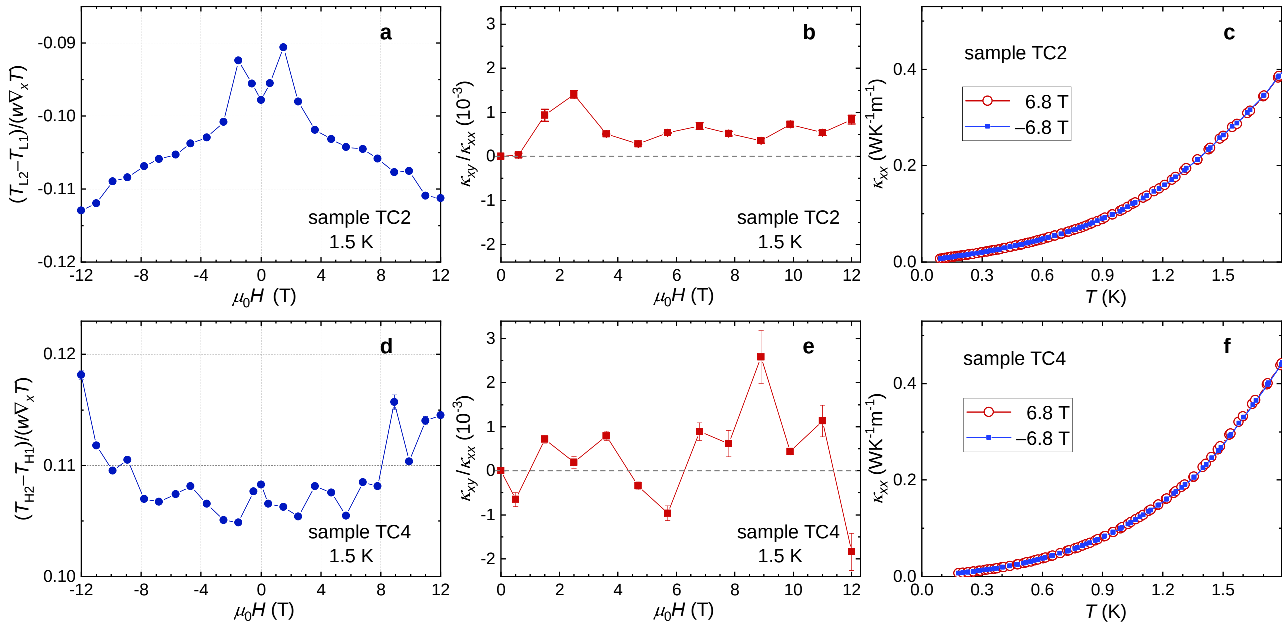

Supplementary Fig. 6 | Magnetic field dependence of longitudinal thermal conductivity and thermal Hall conductivity. **a**, Ratio of transverse to longitude temperature gradients, $(T_{\mathrm{L2}} - T_{\mathrm{L1}})/(w\nabla_x T)$, measured at 1.5 K on sample TC2 (see Supplementary Fig. 1f). **b**, Thermal Hall ratios, κ_{xy}/κ_{xx} ($\equiv \nabla_y T/\nabla_x T$). **c**, Longitudinal thermal conductivity measured at 6.8 T and −6.8 T. **d-f**, Corresponding data measured on sample TC4. In **a**,**b**,**d**,**e**, error bars, 1σ s.e.

been insufficient (see main text). In this work, we successfully identified an elongated single crystal, TC5 (A = 0.056×0.63 mm^2; l_{c} = 0.82 mm)—also oriented along [110] according to Laue XRD—with the highest room-temperature electrical resistivity, ρ^{e}_{xx}(300 K) $\sim$ 11 kΩm, among three crystals with suitable shape and size. Notably, sample TC5 shows more than an order of magnitude higher resistivity than the earlier samples TC1-TC4, which had ρ^{e}_{xx}(300 K) $\sim$ 0.38, 0.30, 0.42, and 0.35 kΩm, respectively. The resistance of TC5 is ~25 MΩ even across a small contact gap of ~0.068 mm, exceeding the optimal measurement range (≤6 MΩ) of the physical property measurement system at 300 K. As a result, precise resistivity data for sample TC5 below 300 K are not available.

The heat leakage of our thermal conductivity setup is negligible for the following reasons:

(1) To minimize heat leakage, we used a cantilever-based thermal conductivity setup that was thermally isolated from all supporting components, except for minor additional heat flow mainly through the NbTi superconducting leads (diameter d_{NbTi} = 63 μm, length l_{NbTi} = 13 mm) connected to the heater and thermometers, as shown in the inset of Supplementary Fig. 7c. Prior to condensing the ^{3}He-^{4}He dilution refrigerator, the exchange helium gas was pumped out at 5-10 K for over 8 hours using a compound turbo

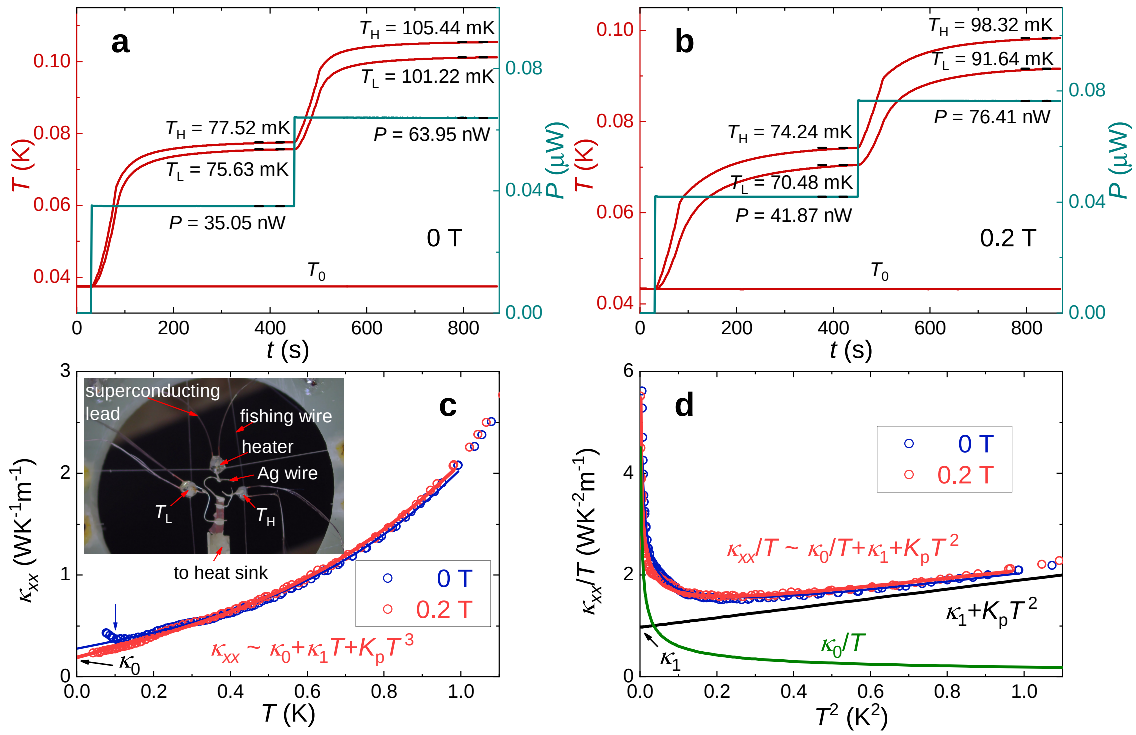

Supplementary Fig. 7 | Thermal conductivity measured on GdZnPO sample TC5. a, **b**, Temperature readings from thermometers (T_{H}, T_{L}, T_0) and heater power (P) during two representative measurements at 0 and 0.2 T. Dashed lines indicate steady-state values used to evaluate $\kappa_{xx}[(T_{\mathrm{H}}+T_{\mathrm{L}})/2]$ = $l_{\mathrm{c}}P/A/(T_{\mathrm{H}}-T_{\mathrm{L}})$, where l_{c} = 0.82 mm is the contact distance and A = 0.056×0.63 mm^2 is the cross-sectional area. Resulting values:—At 0 T: κ_{xx}(76.6 mK) = 0.430 WK^{-1}m^{-1}, κ_{xx}(103.3 mK) = 0.352 WK^{-1}m^{-1}—At 0.2 T: κ_{xx}(72.4 mK) = 0.259 WK^{-1}m^{-1}, κ_{xx}(95.0 mK) = 0.266 WK^{-1}m^{-1}. **c**, Temperature dependence of κ_{xx} at 0 and 0.2 T, fitted with κ_{xx} = $\kappa_0+\kappa_1 T+K_{\mathrm{p}}T^3$ (blue and red lines), below 1 K. The inset shows sample TC5 after the measurements. The vertical arrow marks the upturn onset in zero-field κ_{xx} as T decreases. **d**, Same data re-plotted as κ_{xx}/T vs T^2. The olive and black lines show the κ_0/T and $\kappa_1+K_{\mathrm{p}}T^2$ components of the 0.2 T fit, respectively.

pump (nEXT85D, nXDS6i, Edwards), achieving a high vacuum of ~2.5×10^{-9} bar. We made every effort to suppress heat leakage during the measurements.

(2) A similar experimental setup was previously used to measure the thermal conductivity (κ) of α-CoV_2O_6 single crystals, where magnetic excitations are gapped (~35 K), and phonons dominate thermal transport below 2 K [1]. κ/T decreases rapidly with decreasing temperature, following $\kappa \sim K_{\mathrm{p}}T^3$ down to the lowest measured temperature, indicating negligible heat leakage in our setup. At $\sim$ 0.1 K, we obtained a reasonable thermal conductivity value of $\kappa \sim$ 1 mWK^{-1}m^{-1}, yielding a total heat conductance κ_{total} = $\kappa A/l_{\mathrm{c}} \sim$ 0.1 μWK^{-1} [1]. Therefore, the heat-leakage conductance of our setup at ~0.1 K must be less than ~0.1 μWK^{-1}, which is more than two orders of magnitude smaller than the total heat conductance of the

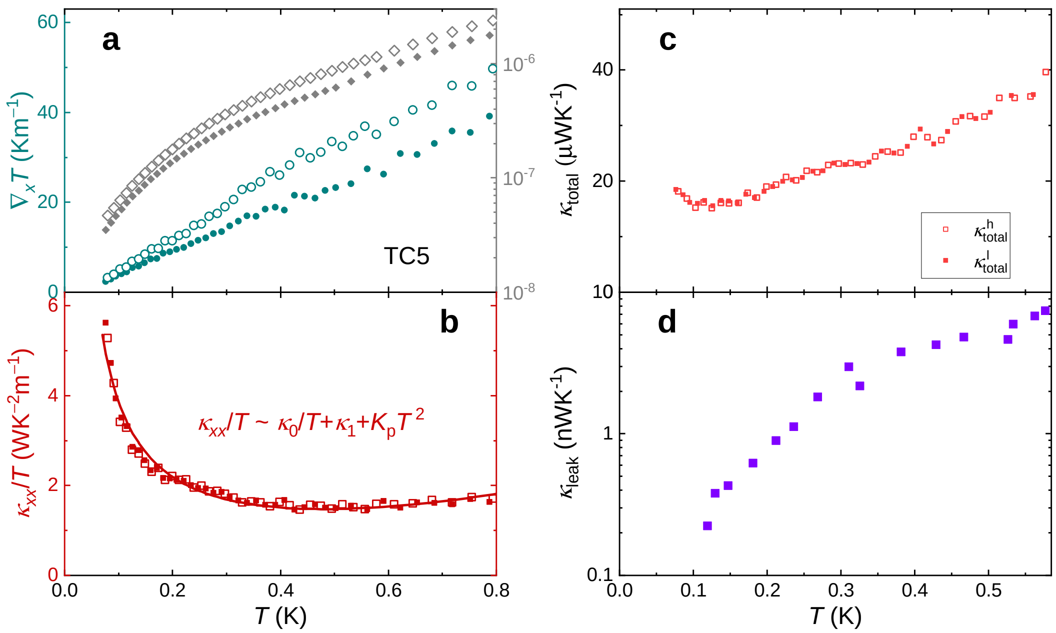

Supplementary Fig. 8 | Raw thermal conductivity data of sample TC5 at 0 T. a, Applied heating power (P) and the resulting longitudinal temperature gradient ($\nabla_x T$). **b**, Thermal conductivity divided by temperature, κ_{xx}/T, with the solid line showing a fit, $\kappa_{xx}/T \sim \kappa_0/T+\kappa_1 + K_\mathrm{p}T^2$, below 1 K. **c**, Total heat conductance between T_H and T_L, $\kappa_\mathrm{total} = P/(T_\mathrm{H} - T_\mathrm{L})$. Solid and open symbols denote data under lower and higher power, respectively. **d**, Heat-leak conductance through six NbTi superconducting leads (diameter d_NbTi = 63 μm, length l_NbTi = 13 mm), calculated as $\kappa_\mathrm{leak} \sim 6\pi\kappa_\mathrm{NbTi}d^2_\mathrm{NbTi}/(4l_\mathrm{NbTi})$, where the thermal conductivity κ_NbTi is adapted from Ref. [2].

GdZnPO sample TC5 (see Supplementary Fig. 8c).

(3) The thermal conductivity of NbTi wire is extremely low at ultra-low temperatures: $\kappa_\mathrm{NbTi} \sim 2\times10^{-6}$ Wcm^{-1}K^{-1} (2×10^{-4} Wm^{-1}K^{-1}) at $\sim$0.1 K and $\sim$ 1×10^{-4} Wcm^{-1}K^{-1} (1×10^{-2} Wm^{-1}K^{-1}) at $\sim$1 K [2]. For our leads, this corresponds to $\kappa_\mathrm{lead} = \pi\kappa_\mathrm{NbTi}d^2_\mathrm{NbTi}/(4l_\mathrm{NbTi}) \sim 5\times10^{-11}$ WK^{-1} at $\sim$0.1 K and $\sim$ 2×10^{-9} WK^{-1} at $\sim$1 K. Even with six leads, the total heat-leak conductance, $\kappa_\mathrm{leak} \sim 6\kappa_\mathrm{lead} \sim 2.9\times10^{-10}$ WK^{-1} at $\sim$0.1 K and $\sim$ 1.4×10^{-8} WK^{-1} at $\sim$1 K (see Supplementary Fig. 8d), is more than three orders of magnitude smaller than the measured heat conductance of GdZnPO (sample TC5), $\kappa_\mathrm{total} \sim 1.7\times10^{-5}$ WK^{-1} at $\sim$0.1 K and $\sim$ 8.8×10^{-5} WK^{-1} at $\sim$1 K, and is more than two orders of magnitude smaller than that of α-CoV_2O_6 (sample no. 1) [1], $\sim$$1\times10^{-7}$ WK^{-1} at $\sim$0.1 K and $\sim$$1\times10^{-4}$ WK^{-1} at $\sim$1 K. Thus, heat leakage through the superconducting leads is negligible.

We used NbTi wires with d_NbTi = 63 μm and l_NbTi = 13 mm, providing robust electrical connections for the thermometers and heater while avoiding short circuits. As discussed above, the resulting heat-leakage conductance is negligibly small, even in thermal-conductivity measurements dominated by phonons (e.g., α-CoV_2O_6 [1]).

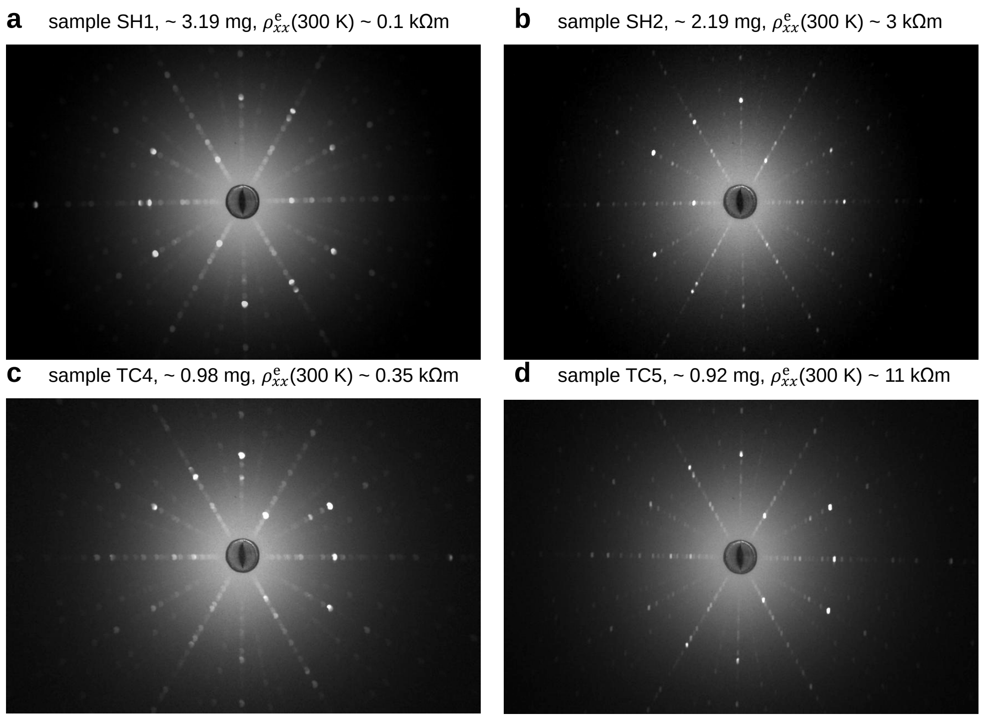

Supplementary Fig. 9 | Laue x-ray diffraction (XRD) patterns of specific-heat samples and thermal-conductivity samples. a-b, Laue patterns measured on the upper surfaces of specific-heat samples SH1 and SH2, and thermal-conductivity samples TC4 and TC5. All measurements were conducted sequentially under identical conditions: tungsten target (20 kV, 15 mA), 400 s exposure, and fixed sample-detector distance. Crystal mass and room-temperature electrical resistivity ρ^{e}_{xx}(300 K) are also listed.

To achieve a high signal-to-noise ratio, we applied a heat power of $P \sim 4{\times}10^{-8}$ W at $\sim$ 0.1 K for GdZnPO sample TC5, producing a relative temperature difference $2(T_{\rm H}-T_{\rm L})/(T_{\rm H}+T_{\rm L}) \sim$ 3-7% (e.g., see Supplementary Fig. 7a,b). Compared to the typical value of $P \sim 6{\times}10^{-10}$ W used in α-CoV_2O_6 at 0.1 K [1], the relatively large P used in this work reflects the unusually high residual κ_{xx} (or $\kappa_{\rm total}$) of GdZnPO, which is associated with the spiral spin liquid (SSL) physics (see the main text).

As shown in Supplementary Fig. 11a,c,e,g and Fig. 3a of the main text, a weak low-temperature upturn in κ_{xx} occurs only for TC5 at 0 T below $\sim$ 0.1 K. For TC1-TC4 and for TC5 at finite fields, κ_{xx} decreases monotonically with decreasing temperature down to the lowest measured temperature ($\kappa_{xx} \sim \kappa_0 + \kappa_1 T + K_{\rm p} T^3$), consistent with the SSL scenario.

Based on Laue XRD photographs (see Supplementary Fig. 9), we find that samples SH1 and TC4 both exhibit relatively poor crystallinity, while SH2 and TC5 show comparably higher crystallinity. The observation of negligible sample dependence in specific heat between SH1 (lower crystallinity) and SH2 (higher), alongside the pronounced sample dependence in thermal conductivity between TC4 (lower) and

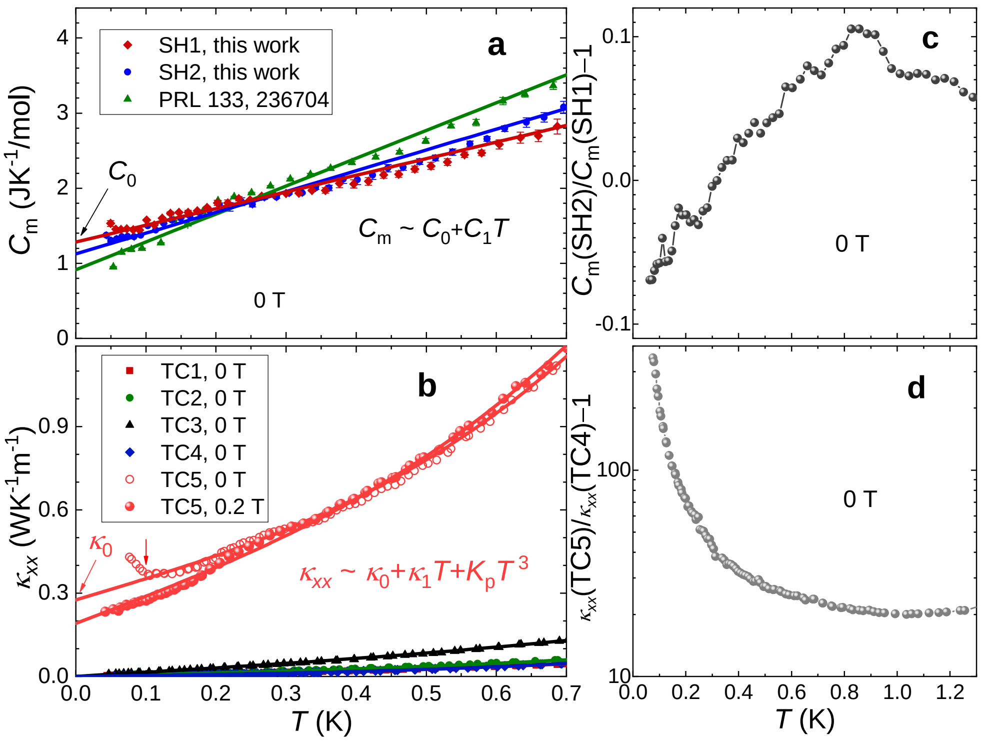

Supplementary Fig. 10 | Sample dependence of specific heat and heat transport properties of GdZnPO. a, Magnetic specific heat (C_m) of samples SH1 and SH2, along with previously reported data. Colored lines represent linear fits using $C_\mathrm{m} = C_0 + C_1T$. **b**, Thermal conductivities of samples TC1-TC5, with colored lines showing the fits, $\kappa_{xx} = \kappa_0 + \kappa_1 T + K_\mathrm{p}T^3$. The vertical arrow indicates the temperature where an upturn in TC5 at 0 T appears as T decreases. **c**, Relative deviation of specific heat: C_m(SH2)/C_m(SH1)-1. **d**, Relative deviation of thermal conductivity: κ_{xx}(TC5)/κ_{xx}(TC4)-1.

TC5 (higher), as shown in Supplementary Fig. 10, together provide a consistent and convincing resolution to the sample dependence issue for GdZnPO.

In the κ_{xx} plots (see Supplementary Fig. 11a,c,e,g), the fits generally agree well with the data, although some deviations appear below $\sim$0.3 K when the data are presented as κ_{xx}/T vs. T^2 (see Supplementary Fig. 11b,d,f,h). Notably, sample TC4, which shows broader Laue patterns (see Supplementary Fig. 9), exhibits κ_{xx}/T values falling below the fitted curve $\kappa_0/T + \kappa_1 + K_\mathrm{p}T^2$ below $\sim$0.3 K (see Supplementary Fig. 11h). Similarly, sample TC2 shows a drop in κ_{xx}/T below $\sim$0.15 K at a high field of $\sim$12 T (see Supplementary Fig. 11d). Such low-temperature suppression of κ/T has also been reported in various magnetic systems, including $PbCuTe_2O_6$ [3], $YbMgGaO_4$ [14], $Na_2Co_2TeO_6$ [15], and $Cu(C_6H_5COO)_2{\cdot}3H_2O$ [16]. This phenomenon has been attributed to spin gap opening, many-body localization, and/or disorder effects that suppress the transport of spin excitations [3, 14–16].

In the case of GdZnPO, the low-temperature drop in κ_{xx}/T is mainly observed in sample TC4, which

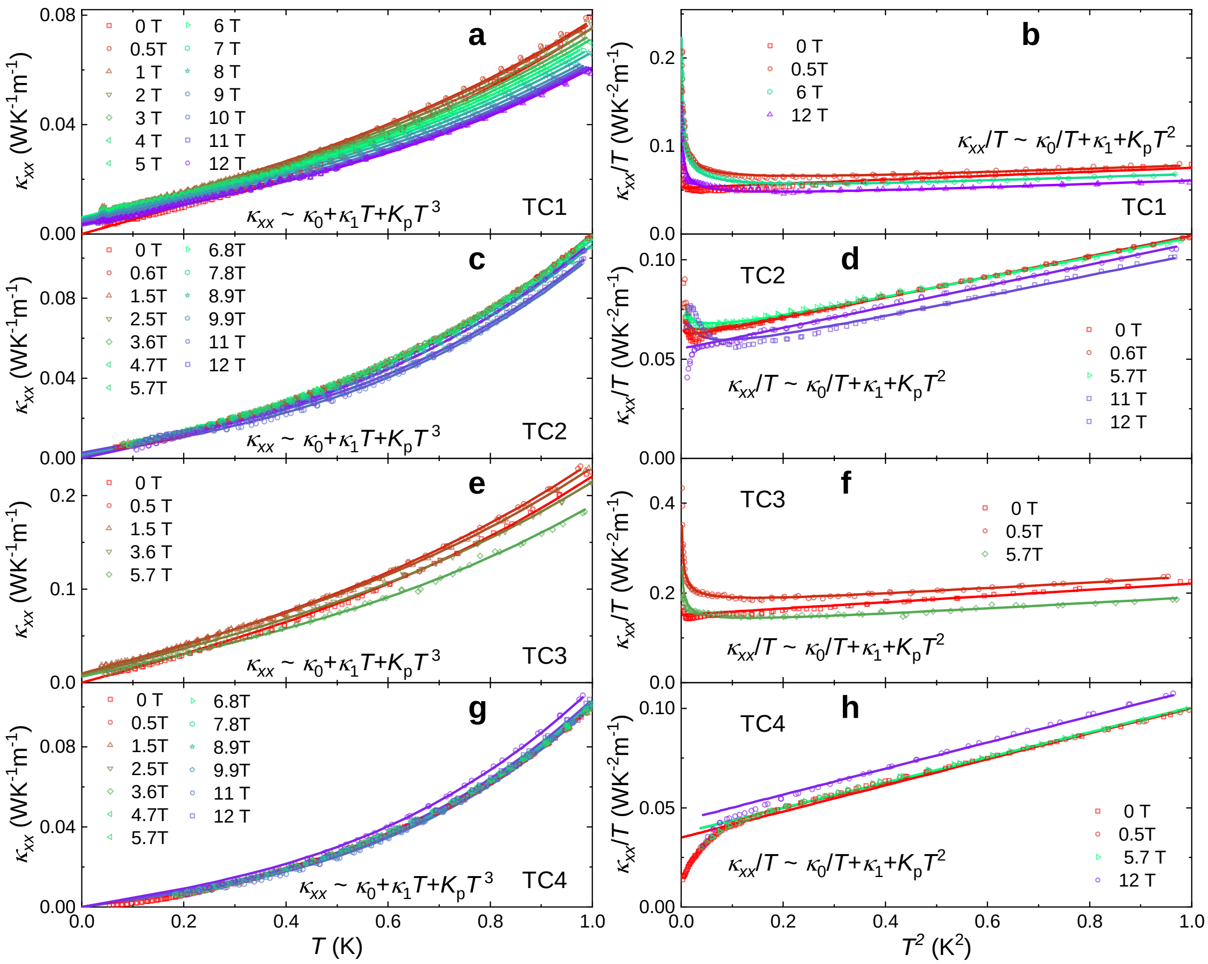

Supplementary Fig. 11 | **Fits to the thermal conductivity data of GdZnPO crystals. a**,**c**,**e**,**g**, Thermal conductivity κ_{xx} of samples TC1-TC4, fitted below 1 K using the expression $\kappa_{xx} \sim \kappa_0 + \kappa_1 T + K_\mathrm{p} T^3$, with all fitted parameters constrained to be non-negative. The extracted values are summarized in Supplementary Fig. 12. **b**,**d**,**f**,**h**, Corresponding plots of κ_{xx}/T versus T^2 for the selected data.

exhibits broader Laue patterns and poorer electrical insulation, suggesting that the suppression is caused by disorder effects. In contrast, the most electrically insulating sample TC5—with sharp Laue photographs (see Supplementary Fig. 9)—shows no such drop (see Fig. 3 in the main text). Instead, its thermal conductivity is well described by $\kappa_{xx} \sim \kappa_0 + \kappa_1 T + K_\mathrm{p} T^3$ below 1 K. Remarkably, in zero field, sample TC5 even exhibits an unusual upturn in κ_{xx} below $\sim$0.1 K. This upturn is suppressed by a small magnetic field of $\sim$0.2 T. A similar phenomenon was previously reported in the Kitaev material $Na_2Co_2TeO_6$, where the low-temperature rise in zero-field κ/T was attributed to the recovery of thermal transport by itinerant excitations at ultra low temperatures [17].

The fitted parameters from the fits below 1 K are summarized in Supplementary Fig. 12, for GdZnPO

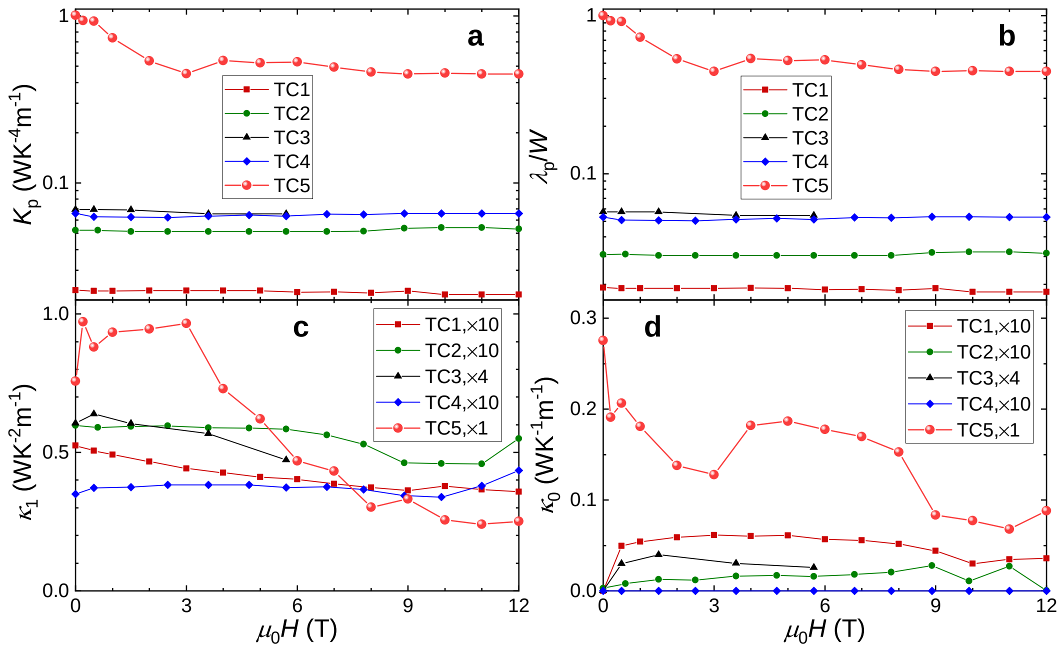

Supplementary Fig. 12 | Fitted parameters from the thermal conductivity data of various GdZnPO crystals below 1 K. The data were fitted using $\kappa_{xx} = \kappa_0 + \kappa_1 T + K_\mathrm{p} T^3$. The optimized phonon coefficient K_p, and magnetic terms κ_1 and κ_0 are shown in panels **a**, **c**, and **d**, respectively. **b**, Ratio of the phonon mean free path to average sample width, λ_p/W, where λ_p is calculated from the fitted K_p in **a**, and $W = 2\sqrt{A/\pi}$ with A the cross-sectional area. The weak field dependence of K_p and λ_p/W may arise from phonon-magnetic excitation scattering, as the GdZnPO spin system is gapless.

samples TC1-TC5. The phonon prefactor K_p, as well as the magnetic terms κ_0 and κ_1, are significantly enhanced in the highest-quality sample TC5.

The low-temperature magnetization of GdZnPO is presented in Supplementary Fig. 13a. If magnetic hysteresis were present, one would expect $M_{\textbf{sweep down}} > M_{\textbf{sweep up}}$ at low temperatures, in contrast to our experimental observations. Therefore, no evident magnetic hysteresis is observed down to at least 50 mK in GdZnPO, consistent with the theoretical expectation of the SSL ansatz for the easy-plane J_1-J_2 honeycomb-lattice model in the classical level at 0 K [18]. Accordingly, it is not necessary to distinguish between magnetization and demagnetization processes when antisymmetrizing the transverse temperature gradient in GdZnPO (see above), in contrast to the case of the ferromagnet VI_3 [19].

As shown in Supplementary Fig. 13a, the measured magnetic susceptibility, dM/dH, remains larger than the Van Vleck susceptibility even at 12 T and 50 mK ($\sim$0.4%$|\theta_\mathrm{w}|$, where $\theta_\mathrm{w} \sim -12$ K is the Curie-Weiss temperature), indicating that the GdZnPO spin system is not fully polarized. Both M and dM/dH exhibit fine features that deviate from classical theoretical predictions as the applied field approaches the

Supplementary Table 1 | Reported phonon mean free paths of various compounds, compared with GdZnPO samples in this work. The cross-section area is A = thickness×full width (in μm^2); average width $W = 2\sqrt{A/\pi}$ (in μm). Listed are the reference phonon mean free path $\lambda_{\mathrm{p}}^{\mathrm{ref}}$ (in μm), phonon coefficient K_{p} (in WK^{-4}m^{-1}) at low temperatures, and the mean free path $\lambda_{\mathrm{p}}^{\mathrm{cal}}$ (in μm) calculated from K_{p}.

compounds	sample no.	thickness×full width	W	$\lambda_{\mathrm{p}}^{\mathrm{ref}}$	K_{p}	$\lambda_{\mathrm{p}}^{\mathrm{cal}}$	λ_{p}/W
$PbCuTe_2O_6$ [3]	S1	720×880	898	5.49	0.0206	7.5	0.0061
	S2	750×1040	997	9.56	-	-	0.0096
	P	200×1220	557	5.13	-	-	0.0092
UO_2 [4]	A<100>	1000×1000	1130	13.1	-	-	0.012
$Na_2Co_2TeO_6$ [5]	A	100×1000	357	42.1	-	-	0.12
	Z	100×1000	357	132	-	-	0.37
$Na_2BaCo(PO_4)_2$ [6]	-	140×630	335	-	0.297	43	0.13
SnSe [7]	-	thickness: 700-1000	-	54	-	-	-
PbS [8]	-	-	-	61	-	-	-
α-CoV_2O_6 [1]	no. 1	110×450	251	120	0.514	120	0.48
	no. 2	150×600	339	-	0.477	116	0.34
$Ho_2Ti_2O_7$ [9]	large (6 T)	340×350	389	190	-	-	0.49
	small (6 T)	100×170	147	101	-	-	0.69
$KBaYb(BO_3)_2$ [10]	A	60×810	249	360	-	-	1.45
	B	80×430	209	300	-	-	1.44
GdZnPO	TC1	170×290	251		0.0229	4.8	0.019
(this work)	TC2	60×1630	353		0.0521	10.9	0.031
	TC3	60×830	252		0.0693	14.5	0.058
	TC4	30×1740	258		0.0657	13.8	0.054
	TC5	56×630	212		0.94	197	0.93

crossover value of 12 T [12]. Similarly, clear discrepancies are observed between the experimental specific heat (see Supplementary Fig. 13b) and the semi-classical spin-wave simulations (see Fig. 4b in the main text). These deviations can be attributed to the finite spin quantum number S = 7/2 of the real GdZnPO system, whereas the current theoretical model employs classical spin vectors (S = +∞) to reduce computational cost. As a result, the total entropy per spin is reduced from an unbounded value in the classical limit to Rln($2S+1$) = $3R$ln2 in the real system, giving rise to quantum fluctuations at low temperatures. While the classical easy-plane J_1-J_2 honeycomb-lattice model predicts a crossover field of $\mu_0 H_{\mathrm{c}}$ = $S[2D+3J_1+9J_2+J_1^2/(4J_2)]/(g\mu_{\mathrm{B}})$ = 12 T between the SSL and the polarized phase [12], a significantly higher field would likely be needed to fully polarize the GdZnPO spin system. Therefore, the

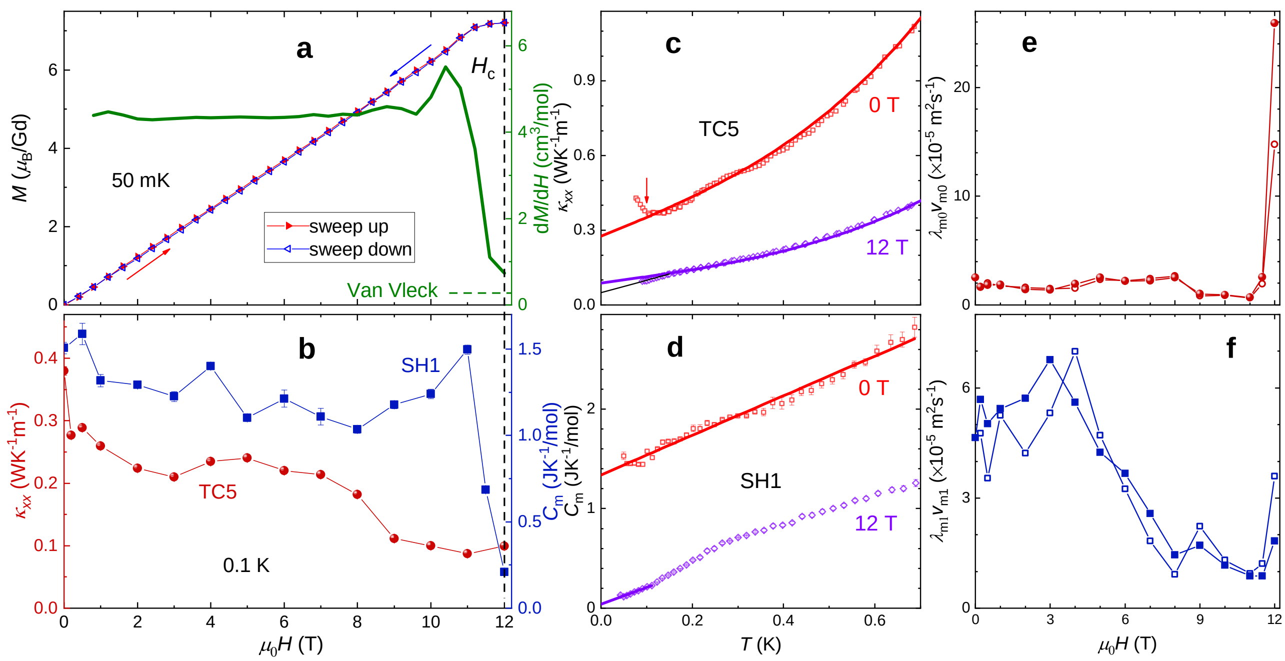

Supplementary Fig. 13 | Field dependence of isothermal magnetization, thermal conductivity, and magnetic specific heat. a, Dc magnetization (M) of GdZnPO measured at 50 mK during field sweeps up (red) and down (blue) using a Faraday force magnetometer [11]. The sold olive line shows dM/dH, with the dashed olive line indicating the Van Vleck susceptibility. **b**, Thermal conductivity of the highest-quality sample TC5 and specific heat of SH1 at 0.1 K. The dashed black line marks the crossover field $\mu_0 H_c \sim 12$ T. **c**, Temperature dependence of thermal conductivity at 0 and 12 T. Colored lines show fits to $\kappa_{xx} = \kappa_0 + \kappa_1 T + K_p T^3$ below 1 K. The thin black line is a linear fit at $T \leq 0.14$ K, where the phonon term $K_p T^3$ (≤ 0.018 WK^{-1}m^{-1}) is negligible. **d**, Magnetic specific heat measured at 0 and 12 T. Colored lines show linear fits ($C_m = C_0 + C_1 T$) below 0.7 and 0.12 K, respectively. The magnetic field is applied along the c axis. **e**, $\lambda_{m0} v_{m0} = 3N_A V_0 \kappa_0 / C_0$. **f**, $\lambda_{m1} v_{m1} = 3N_A V_0 \kappa_1 / C_1$. Here, $V_0 = 67.6$ Å^3 represents the volume per formula. Solid and open symbols show calculations using the fitted values of κ_0 (κ_1) below 1 K and below 0.14 K, respectively (see **c**).

absence of a sharp drop to zero in the low-T κ_{xx} (see Supplementary Fig. 13b) or in the residual κ_0 (see Fig. 3 in the main text) up to 12 T is physically reasonable. In this work, we have successfully measured the specific heat of GdZnPO down to ~0.043 K, revealing the presence of a small residual term even at 12 T, $C_0 = 0.042 \pm 0.01$ JK^{-1}/mol (see Supplementary Fig. 13d). Therefore, the observation of a finite residual thermal conductivity at 12 T (see Supplementary Fig. 13c)—$\kappa_0 \sim 0.05$ WK^{-1}m^{-1} (from the fit below 0.14 K) or 0.09 WK^{-1}m^{-1} (from the fit below 1 K)—does not seem implausible. Unfortunately, our current experimental setup is limited to a maximum magnetic field of 12 T, and ultra-low-temperature measurements beyond this field are not yet available.

The sharp drop in the low-T specific heat near 12 T (see Supplementary Fig. 13b) is primarily attributed

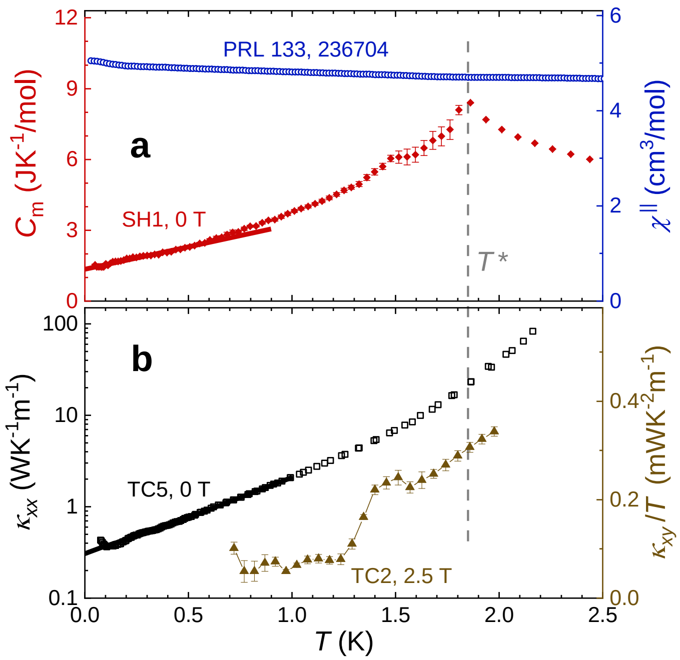

Supplementary Fig. 14 | Thermodynamic and thermal transport properties of GdZnPO. a, Temperature dependence of magnetic specific heat (C_{m}) and magnetic susceptibility measured along the c axis [12]. **b**, Longitudinal thermal conductivity (κ_{xx}) and thermal Hall conductivity (κ_{xy}) measured along the c axis. The dashed line indicates the crossover temperature T^*, corresponding to the peak in C_{m}.

to the suppression of the residual term C_0 (see Fig. 3 in the main text). Therefore, the absence of a sharp drop in the low-T κ_{xx} or in the residual κ_0 should be phenomenologically attributed to a sudden enhancement of the mean free path and/or group velocity of the zero-energy excitations along the SSL counter, $\lambda_{\mathrm{m0}}v_{\mathrm{m0}}$, near $\mu_0 H_{\mathrm{c}} \sim 12$ T (see Supplementary Fig. 13e), likely driven by quantum fluctuations. This observation calls for further theoretical investigation.

As shown in Supplementary Fig. 14a, the temperature dependence of magnetic susceptibility exhibits no evident anomaly near the crossover temperature T^*. In contrast, the classical Monte Carlo simulations of susceptibility display a clear peak or kink at $T^* \sim 2$ K (see Fig. 3b in Ref. [12]), likely associated with the spontaneous breaking of chiral symmetry. Moreover, the simulated specific heat shows a significantly sharper peak at T^* compared to the experimental data for GdZnPO. These discrepancies are most likely due to quantum fluctuations arising from the finite spin quantum number S = 7/2 of Gd^{3+} ions, which reduce the total entropy per site from an infinite value (in the classical limit) to $R\ln(2S+1)$ = $3R\ln 2$. However, existing theoretical and numerical studies of the easy-plane J_1-J_2 honeycomb-lattice model remain at the classical level, and accurate simulations of a frustrated S = 7/2 quantum spin system remain extremely challenging.

Therefore, it is not particularly surprising that no evident anomaly is observed in the temperature dependence of κ_{xx} and κ_{xy}/T around T^*, as shown in in Supplementary Fig. 14b. Even in the experimental specific heat, the peak near $T^* \sim 2$ K is broad, indicating a crossover from the high-temperature paramagnetic phase to the putative SSL of GdZnPO, rather than a sharp phase transition.

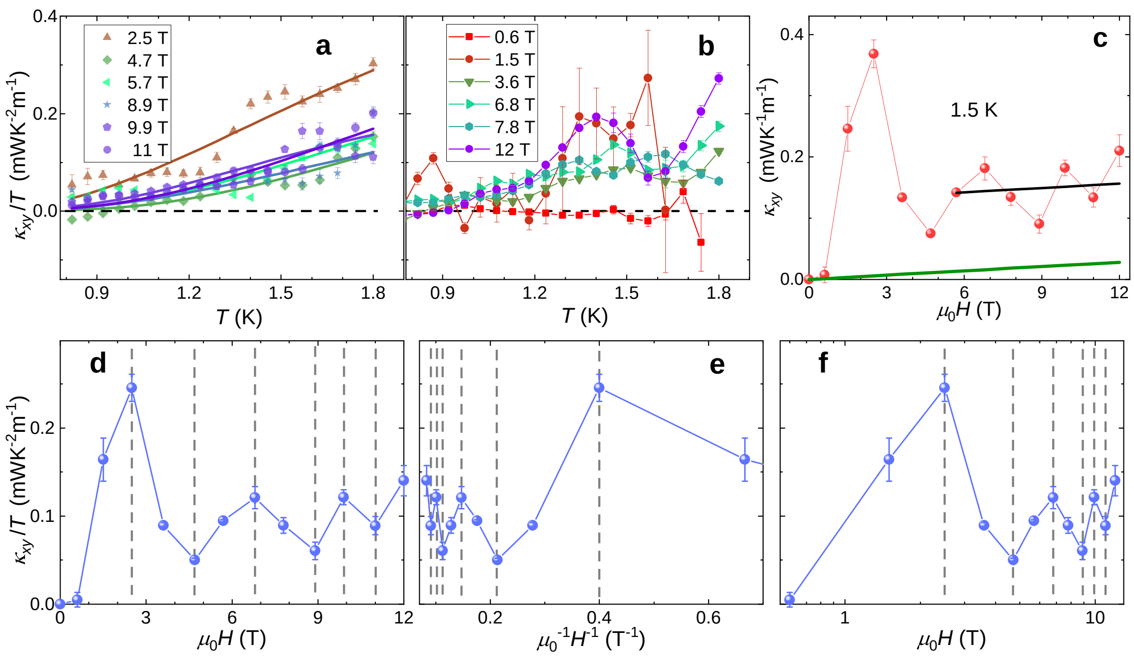

Supplementary Fig. 15 | Thermal Hall conductivity of GdZnPO sample TC2. a, **b**, Temperature dependence of the thermal Hall conductivity (κ_{xy}). The colored lines show the fits using Supplementary Eq. (1), in panel **a**. **c**, Field dependence of thermal Hall conductivity at 1.5 K. The black line shows a linear fit above ∼6 T, $a\mu_0 H + b$, and the olive line represents the estimated phonon contribution $a\mu_0 H$, with a = 2±4 $\times 10^{-6}$ WK^{-1}m^{-1}T^{-1}. **d-f**, Thermal Hall conductivity at T = 1.5 K, plotted as κ_{xy}/T versus $\mu_0 H$, $\mu_0^{-1} H^{-1}$, and $\log_{10}(\mu_0 H)$, respectively. Dashed lines indicate the field values at which κ_{xy}/T exhibits local maxima or minima.

At selected magnetic fields, the thermal Hall conductivity (κ_{xy}) measured on sample TC2 of GdZnPO can be analyzed similarly to Ref. [20]. Notably, at applied fields above ∼1.5 T, κ_{xy}/T increases with rising temperature, reaching significant values above ∼1.2 K (see Supplementary Fig. 15a,b). These observations suggest that the excitations are bosonic. Using the two-flat-band approximation [20], the experimental κ_{xy} can be approximately fitted by,

$$\frac{\kappa_{xy}}{T} = \frac{k_{\mathrm{B}}^2 C_s}{h d_{\mathrm{inter}}}\left[\int_{\frac{\hbar\omega_1}{k_{\mathrm{B}}T}}^{\infty} \frac{x^2 e^x}{(e^x-1)^2}\mathrm{d}x - \int_{\frac{\hbar\omega_2}{k_{\mathrm{B}}T}}^{\infty} \frac{x^2 e^x}{(e^x-1)^2}\mathrm{d}x\right], \tag{1}$$

where $\pm C_s$ is the Chern number of the lower (ω_1) or higher (ω_2) band, respectively, and d_{inter} = c/3 (∼10.2 Å) is the average interlayer distance between neighboring GdO honeycomb layers in GdZnPO [12]. By fitting the data at 2.5, 4.7, 5.7, 8.9, 9.9, and 11 T (see Supplementary Fig. 15a), we obtained C_s = 1.18, 1.13, 0.99, 0.67, 1.21, and 1.13, $\hbar\omega_1$ = 5.4, 7.9, 6.8, 6.4, 6.5, and 6.9 K, $\hbar\omega_2$ = 16, 28, 27, 30, 10, and 28 K, respectively. The fitted C_s values are close to the integer value "1", supporting the validity of the two-flat-band model analysis [20]. The fitted values of $\hbar\omega_1$ and $\hbar\omega_2$ values are nearly an order of magnitude lower than the phonon energies, characterized by the Debye and Einstein temperatures, Θ_{D} and $\Theta_{\mathrm{E}n}$ (n = 1, 2, 3, see Supplementary Fig. 16).

The energy scale of phonons (characterized by the Debye temperature, >100 K) is significantly higher than that of spin excitations (given by the absolute value of the Curie-Weiss temperature, $\sim$12 K) in the oxide GdZnPO. Therefore, the phonon contribution to the thermal Hall effect is generally expected to be small at low temperatures ($\leq$2 K). For example, in $SrTiO_3$ at low temperatures, the phonon thermal Hall conductivity behaves as $\kappa_{xy}^{\mathrm{p}} \sim -a_0T^4$, with $a_0 \sim 8.4\times10^{-4}$ mWK^{-5}m^{-1} at 12 T [21]. At T = 1.5 K, this yields $\kappa_{xy}^{\mathrm{p}} \sim -0.0043$ mWK^{-1}m^{-1}, whose absolute value is more than one order of magnitude smaller than the observed $\kappa_{xy} \sim$ 0.15 mWK^{-1}m^{-1} at 12 T in GdZnPO (see Supplementary Fig. 15c).

Since the energy scale associated with $\sim$12 T (Zeeman energy $\sim$ 10 K) is much smaller than that of phonons (>100 K), a linear field dependence of the phonon thermal Hall conductivity, $\kappa_{xy}^{\mathrm{p}} \sim a\mu_0H$, is generally expected below $\sim$12 T within the linear response approximation—see, for example, Fig. 1(d) in Ref. [21]. Here, a is constant. We performed a linear fit to the high-field κ_{xy} data using the form $a\mu_0H + b$. The estimated phonon contribution, $a\mu_0H$, remains significantly smaller than the measured κ_{xy} across the entire field range (see Supplementary Fig. 15c).

While a periodic thermal Hall effect in $\mu_0^{-1}H^{-1}$ has been reported in CsV_3Sb_5 [22], no convincing periodicity in μ_0H, $\mu_0^{-1}H^{-1}$, or $\log_{10}(\mu_0H)$ is observed in the GdZnPO sample TC2 (see Supplementary Fig. 15d-f). Therefore, it is more likely that the oscillation-like feature arises from normal measurement noise.

Supplementary Note 2. Lattice specific heat

The magnetic specific heat of GdZnPO (see the main text) was obtained by subtracting the lattice contribution, estimated from the specific heat of the nonmagnetic reference compound YZnPO (Supplementary Fig. 16). The specific heat of YZnPO can be fitted using a Debye-Einstein model similar to that in Refs. [1, 23, 24],

$$C_{\mathrm{la}} = \frac{3w_0RT^3}{Z\Theta_{\mathrm{D}}^3}\int_0^{\frac{\Theta_{\mathrm{D}}}{T}} \frac{\xi^4e^{\xi}}{(e^{\xi}-1)^2}\mathrm{d}\xi + \frac{R}{ZT^2}\sum_{n=1}^{3}\frac{w_n\Theta_{\mathrm{E}n}^2e^{\frac{\Theta_{\mathrm{E}n}}{T}}}{(e^{\frac{\Theta_{\mathrm{E}n}}{T}}-1)^2}, \tag{2}$$

where Z = 6 represents the number of formulas per unit cell of YZnPO (or GdZnPO), and the weight factors

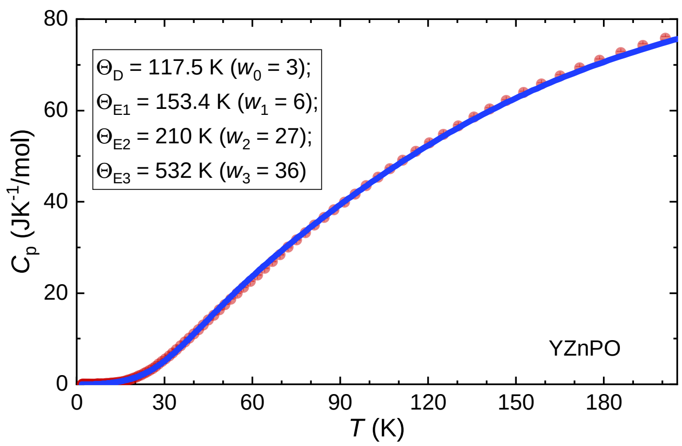

Supplementary Fig. 16 | Specific heat of the nonmagnetic reference compound YZnPO. The blue line shows the fit using the Debye-Einstein lattice model (see Supplementary Eq. (2)), with the fitted parameters listed. Error bars, 1σ s.e.

w_0 = 3, w_1 = 6, w_2 = 27, w_3 = 36 are fixed ($w_0 + w_1 + w_2 + w_3$ = 3×4×Z) for simplicity. The fitted Debye and Einstein temperatures, Θ_D and Θ_En, are listed in Supplementary Fig. 16. At $T \ll \Theta_\mathrm{D}$ (∼117.5 K), the lattice specific heat (per mole formula) is proportional to T^3, $C_\mathrm{la} \simeq \frac{12\pi^4 RT^3}{5Z\Theta_\mathrm{D}^3}$ ($C_\mathrm{la}T^{-3} \simeq$ 1.997 $\times 10^{-4}$ JK^{-4}/mol), where R = 8.314 JK^{-1}/mol is the gas constant.

Supplementary Note 3. Linear spin-wave theory for the spiral spin liquid

Under a magnetic field (H) applied along the c axis, the S = 7/2 Hamiltonian of GdZnPO can be approximated as [12]

$$\mathcal{H} = J_1 \sum_{\langle j0,j1\rangle} \mathbf{S}_{j0} \cdot \mathbf{S}_{j1} + J_2 \sum_{\langle\langle j0,j2\rangle\rangle} \mathbf{S}_{j0} \cdot \mathbf{S}_{j2} + D \sum_{j0} (S^z_{j0})^2 - \mu_0 H g \mu_\mathrm{B} \sum_{j0} S^z_{j0}, \quad (3)$$

where $J_1 \sim -0.39$ K and $J_2 \sim 0.57$ K denote the first ($\langle\ \rangle$) and second ($\langle\langle\ \rangle\rangle$) nearest-neighbor couplings, respectively, $D \sim 0.30$ K represents the easy-plane anisotropy, and $g \sim 2$ is the g factor. The combination of J_1 and J_2 induces spin frustration on the honeycomb lattice. At the classical level, the ground-state state of Supplementary Eq. (3) is expected to be a SSL [18], with

$$\mathbf{S}_j^A = S[\cos\psi\cos(\mathbf{Q}\cdot\mathbf{R}_j), \cos\psi\sin(\mathbf{Q}\cdot\mathbf{R}_j), \sin\psi] \text{ and} \quad (4)$$

$$\mathbf{S}_j^B = S[\cos\psi\cos(\mathbf{Q}\cdot\mathbf{R}_j + \phi), \cos\psi\sin(\mathbf{Q}\cdot\mathbf{R}_j + \phi), \sin\psi], \quad (5)$$

for spins on the sublattices A and B of the honeycomb lattice, respectively, where $\mathbf{Q}$ = $h\mathbf{b}_1$+$k\mathbf{b}_2$ is the ordering wave vector, $\mathbf{b}_1$ and $\mathbf{b}_2$ are the reciprocal lattice vectors, and $\mathbf{R}_j$ denotes the position vector of the

j-th unit cell. Using this ansatz, we calculate the system's energy per site as

$$E = (D + \frac{3J_1}{2} + 3J_2)S^2 \sin^2\psi + h_Z S \sin\psi + \frac{J_1 S^2 \cos^2\psi}{2}[\cos\phi + \cos(\phi - 2\pi h) + \cos(\phi - 2\pi h - 2\pi k)] + J_2 S^2 \cos^2\psi[\cos(2\pi h) + \cos(2\pi k) + \cos(2\pi h + 2\pi k)], \quad (6)$$

where $h_Z = -\mu_0 H g \mu_B$. By minimizing Supplementary Eq. (6), the angles ϕ and ψ are determined as $\cos\phi = \frac{f_1}{\sqrt{f_1^2+f_2^2}}$, $\sin\phi = \frac{f_2}{\sqrt{f_1^2+f_2^2}}$, and $\sin\psi = -\frac{h_Z}{2S\eta}$. Here, $f_1 = 1 + \cos(2\pi h_G) + \cos(2\pi h_G + 2\pi k_G)$, $f_2 = \sin(2\pi h_G) + \sin(2\pi h_G + 2\pi k_G)$, and $\eta = D + \frac{3J_1}{2} + \frac{J_1^2}{8J_2} + \frac{9J_2}{2}$, along with the degenerate spiral contour,

$$\cos(2\pi h_G) + \cos(2\pi k_G) + \cos(2\pi h_G + 2\pi k_G) = \frac{1}{2}(\frac{J_1^2}{4J_2^2} - 3). \quad (7)$$

Using the ground state described in Supplementary Eqs. (4) and (5), a new spin coordinate system for $\mathbf{S}'$ is defined as

$$\mathbf{S}_j^A = R^z(\mathbf{Q}\cdot\mathbf{R}_j)R^y(\pi/2-\psi)\mathbf{S'}_j^A \text{ and} \quad (8)$$

$$\mathbf{S}_j^B = R^z(\mathbf{Q}\cdot\mathbf{R}_j + \phi)R^y(\pi/2-\psi)\mathbf{S'}_j^B, \quad (9)$$

where $R^\alpha(\theta)$ denotes a spin rotation operator about the α axis ($\alpha = y$ or z) by an angle θ. The spin Hamiltonian in Supplementary Eq. (3) is then expressed in the $\mathbf{S}'$ coordinate system as

$$\begin{aligned}
\mathcal{H} = J_1 \sum_{\langle j0,j1\rangle} \{&[\sin^2\psi\cos(\mathbf{Q}\cdot\mathbf{R}_{j1} - \mathbf{Q}\cdot\mathbf{R}_{j0} + \phi) + \cos^2\psi]S'^x_{j0}S'^x_{j1} + \cos(\mathbf{Q}\cdot\mathbf{R}_{j1} - \mathbf{Q}\cdot\mathbf{R}_{j0} + \phi)S'^y_{j0}S'^y_{j1} \\
&+ [\cos^2\psi\cos(\mathbf{Q}\cdot\mathbf{R}_{j1} - \mathbf{Q}\cdot\mathbf{R}_{j0} + \phi) + \sin^2\psi]S'^z_{j0}S'^z_{j1} - \sin\psi\sin(\mathbf{Q}\cdot\mathbf{R}_{j1} - \mathbf{Q}\cdot\mathbf{R}_{j0} + \phi)(S'^x_{j0}S'^y_{j1} - S'^y_{j0}S'^x_{j1})\} \\
&+ J_2 \sum_{\langle\langle j0,j2\rangle\rangle} \{[\sin^2\psi\cos(\mathbf{Q}\cdot\mathbf{R}_{j2} - \mathbf{Q}\cdot\mathbf{R}_{j0}) + \cos^2\psi]S'^x_{j0}S'^x_{j2} + \cos(\mathbf{Q}\cdot\mathbf{R}_{j2} - \mathbf{Q}\cdot\mathbf{R}_{j0})S'^y_{j0}S'^y_{j2} \\
&+ [\cos^2\psi\cos(\mathbf{Q}\cdot\mathbf{R}_{j2} - \mathbf{Q}\cdot\mathbf{R}_{j0}) + \sin^2\psi]S'^z_{j0}S'^z_{j2} - \sin\psi\sin(\mathbf{Q}\cdot\mathbf{R}_{j2} - \mathbf{Q}\cdot\mathbf{R}_{j0})(S'^x_{j0}S'^y_{j2} - S'^y_{j0}S'^x_{j2})\} \\
&+ D\sum_{j0}[\sin^2\psi(S'^z_{j0})^2 + \cos^2\psi(S'^x_{j0})^2] + h_Z\sin\psi\sum_{j0}S'^z_{j0} + (S'^x_{j0}S'^z_{j1}, S'^y_{j0}S'^z_{j1}, S'^x_{j0}S'^z_{j2}, S'^y_{j0}S'^z_{j2} \text{ terms}).
\end{aligned} \quad (10)$$

We apply the Holstein-Primakoff transformation,

$$S'^{A+}_j \simeq \sqrt{2S}a_j, S'^{A-}_j \simeq \sqrt{2S}a_j^\dagger, S'^{Az}_j = S - a_j^\dagger a_j, \quad (11)$$

$$S'^{B+}_j \simeq \sqrt{2S}b_j, S'^{B-}_j \simeq \sqrt{2S}b_j^\dagger, S'^{Bz}_j = S - b_j^\dagger b_j, \quad (12)$$

where $a_j^\dagger$ and $b_j^\dagger$ (a_j and b_j) are bosonic creation (annihilation) operators, and $S_j'^{\pm} \equiv S_j'^{x} \pm i S_j'^{y}$. Performing the Fourier transformation, we derive the spin-wave Hamiltonian,

$$\mathcal{H}_{\rm sw} = \frac{1}{2}\sum_{\mathbf{k}} \Psi^\dagger(\mathbf{k})\mathcal{H}(\mathbf{k})\Psi(\mathbf{k}), \tag{13}$$

where $\Psi(\mathbf{k}) = [a(\mathbf{k}); b(\mathbf{k}); a^\dagger(-\mathbf{k}); b^\dagger(-\mathbf{k})]$. At $\mathbf{Q} = \mathbf{Q}_{\rm G} \equiv h_{\rm G}\mathbf{b}_1 + k_{\rm G}\mathbf{b}_2$, the Bogoliubov-de Gennes (BdG) Hamiltonian adopts the general form,

$$\mathcal{H}(\mathbf{k}) = \begin{bmatrix} \Xi(\mathbf{k},\mathbf{Q}_{\rm G}) & \Pi(\mathbf{k},\mathbf{Q}_{\rm G}) \\ \Pi^*(-\mathbf{k},\mathbf{Q}_{\rm G}) & \Xi^*(-\mathbf{k},\mathbf{Q}_{\rm G}) \end{bmatrix}, \tag{14}$$

with

$$\Xi(\mathbf{k},\mathbf{Q}_{\rm G}) = \Xi^0(\mathbf{k},\mathbf{Q}_{\rm G})\sigma_0 + \Xi^x(\mathbf{k},\mathbf{Q}_{\rm G})\sigma_x + \Xi^y(\mathbf{k},\mathbf{Q}_{\rm G})\sigma_y, \tag{15}$$

$$\Pi(\mathbf{k},\mathbf{Q}_{\rm G}) = \Pi^0(\mathbf{k},\mathbf{Q}_{\rm G})\sigma_0 + \Pi^x(\mathbf{k},\mathbf{Q}_{\rm G})\sigma_x + \Pi^y(\mathbf{k},\mathbf{Q}_{\rm G})\sigma_y. \tag{16}$$

Here, $\sigma_0 = \begin{bmatrix} 1 & 0 \\ 0 & 1 \end{bmatrix}$, $\sigma_x = \begin{bmatrix} 0 & 1 \\ 1 & 0 \end{bmatrix}$, and $\sigma_y = \begin{bmatrix} 0 & -i \\ i & 0 \end{bmatrix}$ represent Pauli matrices. Using Supplementary Eqs. (10)-(13), we determine all the prefactors in Supplementary Eqs. (15) and (16),

$$\begin{aligned}\Xi^0 = &-J_1 S\sum_{\mathbf{R}_{01}}[\cos^2\psi\cos(\mathbf{Q}_{\rm G}\cdot\mathbf{R}_{01}+\phi)+\sin^2\psi] - J_2 S\sum_{\mathbf{R}_{02}}\{\sin\psi\sin(\mathbf{Q}_{\rm G}\cdot\mathbf{R}_{02})\sin(\mathbf{k}\cdot\mathbf{R}_{02})+\cos^2\psi\cos(\mathbf{Q}_{\rm G}\cdot\mathbf{R}_{02}) \\ &+\sin^2\psi - \frac{1}{2}[(1+\sin^2\psi)\cos(\mathbf{Q}_{\rm G}\cdot\mathbf{R}_{02})+\cos^2\psi]\cos(\mathbf{k}\cdot\mathbf{R}_{02})\} + DS(1-3\sin^2\psi) - h_{\rm Z}\sin\psi,\end{aligned} \tag{17}$$

$$\Xi^x = \frac{J_1 S}{2}\sum_{\mathbf{R}_{01}}\{[(1+\sin^2\psi)\cos(\mathbf{Q}_{\rm G}\cdot\mathbf{R}_{01}+\phi)+\cos^2\psi]\cos(\mathbf{k}\cdot\mathbf{R}_{01}+\mathbf{k}\cdot\delta) - 2\sin\psi\sin(\mathbf{Q}_{\rm G}\cdot\mathbf{R}_{01}+\phi)\sin(\mathbf{k}\cdot\mathbf{R}_{01}+\mathbf{k}\cdot\delta)\}, \tag{18}$$

$$\Xi^y = \frac{J_1 S}{2}\sum_{\mathbf{R}_{01}}\{[(1+\sin^2\psi)\cos(\mathbf{Q}_{\rm G}\cdot\mathbf{R}_{01}+\phi)+\cos^2\psi]\sin(\mathbf{k}\cdot\mathbf{R}_{01}+\mathbf{k}\cdot\delta) + 2\sin\psi\sin(\mathbf{Q}_{\rm G}\cdot\mathbf{R}_{01}+\phi)\cos(\mathbf{k}\cdot\mathbf{R}_{01}+\mathbf{k}\cdot\delta)\}, \tag{19}$$

$$\Pi^0 = \frac{J_2 S}{2}\cos^2\psi\sum_{\mathbf{R}_{02}}[1-\cos(\mathbf{Q}_{\rm G}\cdot\mathbf{R}_{02})]\cos(\mathbf{k}\cdot\mathbf{R}_{02}) + DS\cos^2\psi, \tag{20}$$

$$\Pi^x = \frac{J_1 S}{2}\sum_{\mathbf{R}_{01}}[(\sin^2\psi-1)\cos(\mathbf{Q}_{\rm G}\cdot\mathbf{R}_{01}+\phi)+\cos^2\psi]\cos(\mathbf{k}\cdot\mathbf{R}_{01}+\mathbf{k}\cdot\delta), \tag{21}$$

$$\Pi^y = \frac{J_1 S}{2}\sum_{\mathbf{R}_{01}}[(\sin^2\psi-1)\cos(\mathbf{Q}_{\rm G}\cdot\mathbf{R}_{01}+\phi)+\cos^2\psi]\sin(\mathbf{k}\cdot\mathbf{R}_{01}+\mathbf{k}\cdot\delta), \tag{22}$$

where $\mathbf{R}_{01}$ = [0;0], [-1;0], [-1;-1] denote the vectors between unit cells for J_1, $\mathbf{R}_{02}$ = [1;0], [1;1], [0;1], [-1;0], [-1;-1], [0;-1] are the vectors between unit cells for J_2, and δ = [2/3;1/3] represents the vector from the A site to the B site within a unit cell. The BdG Hamiltonian in Supplementary Eq. (14) can be diagonalized using a paraunitary matrix $\mathcal{T}(\mathbf{k})$, which satisfies

$$\mathcal{T}^{\dagger}(\mathbf{k})\begin{bmatrix}1&0&0&0\\0&1&0&0\\0&0&-1&0\\0&0&0&-1\end{bmatrix}\mathcal{T}(\mathbf{k})=\begin{bmatrix}1&0&0&0\\0&1&0&0\\0&0&-1&0\\0&0&0&-1\end{bmatrix}, \tag{23}$$

and

$$\mathcal{T}^{\dagger}(\mathbf{k})\mathcal{H}(\mathbf{k})\mathcal{T}(\mathbf{k})=\begin{bmatrix}\hbar\omega_1(\mathbf{k})&0&0&0\\0&\hbar\omega_2(\mathbf{k})&0&0\\0&0&\hbar\omega_1(-\mathbf{k})&0\\0&0&0&\hbar\omega_2(-\mathbf{k})\end{bmatrix}. \tag{24}$$

Here, $\hbar\omega_1(\mathbf{k})$ and $\hbar\omega_2(\mathbf{k})$ (see Supplementary Fig. 17) match exactly with the calculations performed using SpinW in MATLAB [25].

For each $\mathbf{Q}_{\mathrm{G}}$, there are two energy dispersions, $\hbar\omega_1$($\mathbf{k}$,$\mathbf{Q}_{\mathrm{G}}$) and $\hbar\omega_2$($\mathbf{k}$,$\mathbf{Q}_{\mathrm{G}}$), with $\omega_1 \leq \omega_2$, since each unit cell hosts two spins on the honeycomb lattice. When $h_{\mathrm{Z}} \leq 2S\eta$, ω_1 exhibits a zero gap at the Γ point ($\mathbf{k}$ = 0), while displaying a local minimum near the K point–an effect attributed to the easy-plane anisotropy ($D > 0$). Consequently, ω_1 near the Γ point predominantly influences the low-temperature thermodynamic properties due to the Bose-Einstein distribution.

Similar to the Debye specific-heat model, we first determine the maximum frequency ω_{m} by integrating over the wave vector $\mathbf{k}$ across the first Brillouin zone (FBZ) and integrating $\mathbf{Q}_{\mathrm{G}}$ along the degenerate spiral contour within the FBZ,

$$N(\frac{2}{\sqrt{3}})^{\frac{3}{2}}\int_{\mathbf{k},\mathbf{Q}_{\mathrm{G}}\in\mathrm{FBZ}}[\omega_1(\mathbf{k},\mathbf{Q}_{\mathrm{G}})\leq\omega_{\mathrm{m}}]\mathrm{d}\mathbf{k}\mathrm{d}\mathbf{Q}_{\mathrm{G}}=1, \tag{25}$$

where N ($\to\infty$) denotes the number of unit cells along the a or b axis (accounting for a total of $2N^2$ spins), and $|\mathbf{b}_1|$ = $|\mathbf{b}_2|$ = 1.

As a result, the low-temperature specific heat per mole of spins (see Supplementary Fig. 18a) is calculated as

$$C_{\mathrm{m}}^{\mathrm{cal}}=\frac{RN}{2}(\frac{2}{\sqrt{3}})^{\frac{3}{2}}\int_{\mathbf{k},\mathbf{Q}_{\mathrm{G}}\in\mathrm{FBZ}}[\omega_1(\mathbf{k},\mathbf{Q}_{\mathrm{G}})\leq\omega_{\mathrm{m}}]\frac{(\frac{\hbar\omega_1}{k_{\mathrm{B}}T})^2e^{\frac{\hbar\omega_1}{k_{\mathrm{B}}T}}}{(e^{\frac{\hbar\omega_1}{k_{\mathrm{B}}T}}-1)^2}\mathrm{d}\mathbf{k}\mathrm{d}\mathbf{Q}_{\mathrm{G}}. \tag{26}$$

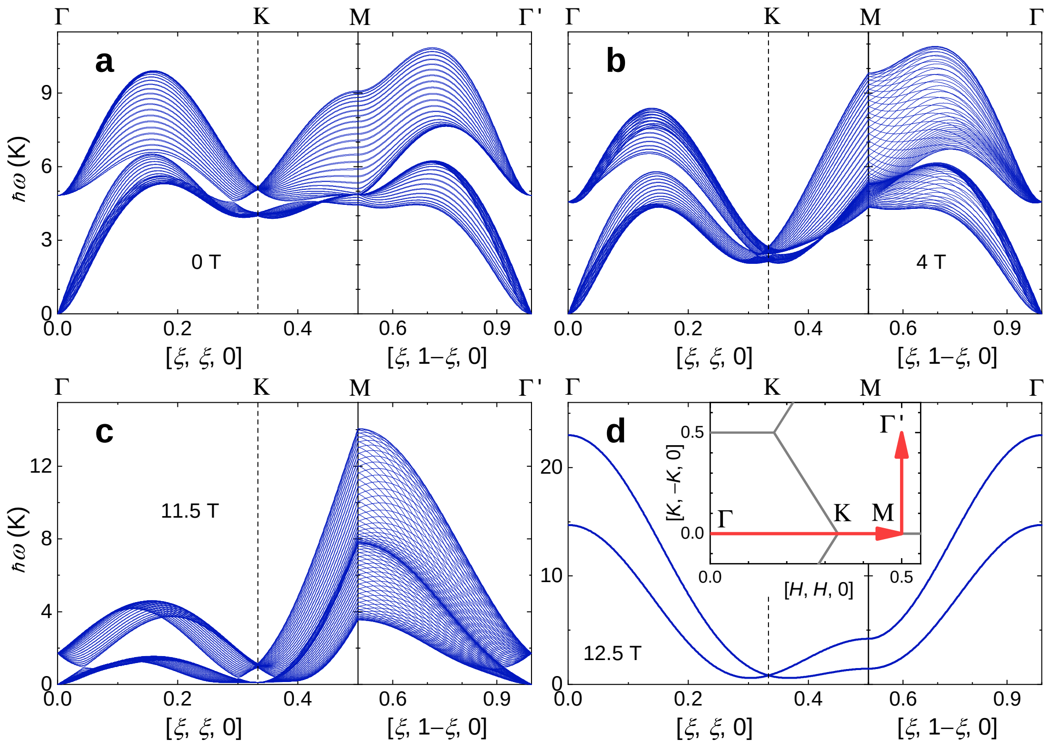

Supplementary Fig. 17 | Energy dispersions calculated using the linear spin-wave approximate at $\mu_0 H$ = 0 T (**a**), 4 T (**b**), 11.5 T (**c**), and 12.5 T (**d**). In **a**-**c**, the spin system is in the spiral spin liquid with $\mu_0 H < \mu_0 H_c$ = $S[2D + 3J_1 + 9J_2 + J_1^2/(4J_2)]/(g\mu_B)$ ($\sim$ 12 T), while the system is fully polarized in **d**. The calculations are based on the determined spin Hamiltonian of GdZnPO [12]. The inset in **d** shows the high-symmetry directions with special **Q** points labeled, and the grey lines indicate Brillouin zone boundaries.

As $N \to \infty$, $\omega_m \to 0$, making the low-temperature C_m^{cal} predominantly influenced by the zero-energy excitations along the spiral contour, as shown in Supplementary Fig. 18a. The average number of magnons is given as

$$n_m = N(\frac{2}{\sqrt{3}})^{\frac{3}{2}} \int_{\mathbf{k},\mathbf{Q}_G \in \mathrm{FBZ}} \frac{\omega_1(\mathbf{k},\mathbf{Q}_G) \le \omega_m}{e^{\frac{\hbar\omega_1}{k_B T}} - 1} d\mathbf{k} d\mathbf{Q}_G. \tag{27}$$

Consequently, the mean magnon velocity along [110] (see Supplementary Fig. 18b,c) is obtained as

$$v_{m1}^{cal} = \frac{N}{n_m}(\frac{2}{\sqrt{3}})^{\frac{3}{2}} \int_{\mathbf{k},\mathbf{Q}_G \in \mathrm{FBZ}} \frac{\omega_1(\mathbf{k},\mathbf{Q}_G) \le \omega_m}{e^{\frac{\hbar\omega_1}{k_B T}} - 1} |(\frac{d\omega_1}{dk})_{[110]}| d\mathbf{k} d\mathbf{Q}_G. \tag{28}$$

The calculated C_m^{cal} and v_{m1}^{cal}, using Supplementary Eqs. (26) and (28), exhibit negligible dependence on the system size N for $N \ge$ 10,000 above ~0.1 K. Therefore, we present the calculations for N = 30,000 in the main text and supplementary information. For $h_Z < 2S\eta$ (i.e., $H < H_c$, with $\mu_0 H_c \sim$ 12 T), the low-energy excitations of the spin system remain gapless at the Γ point, as shown in Supplementary Fig. 17a-c,

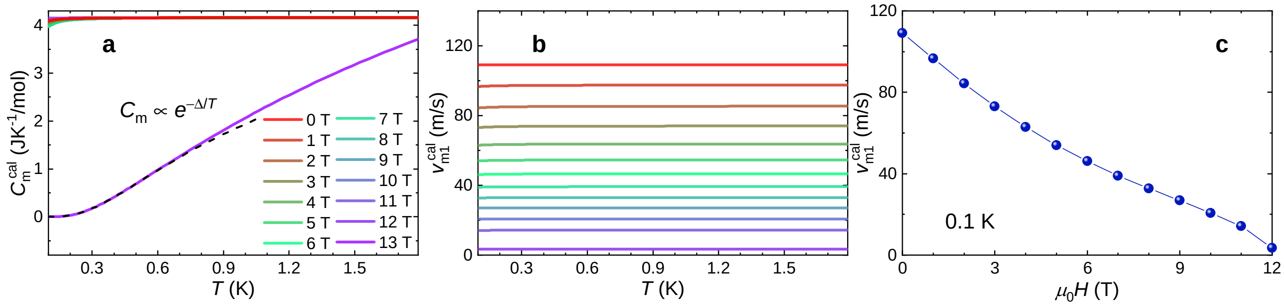

Supplementary Fig. 18 | Low-temperature specific heat and mean magnon velocity calculated using the linear spin-wave approximation for GdZnPO. a, Specific heat (C_{m}), with the dashed black line showing the gap behavior, $C_{\mathrm{m}} \propto \exp(-\Delta/T)$, where $\Delta \sim 1$ K. **b**, Temperature dependence of mean magnon velocity. **c**, Field dependence of mean magnon velocity at 0.1 K.

and $C_{\mathrm{m}}^{\mathrm{cal}}$ remains large between 0.1 and 1.8 K. The low-T value of $C_{\mathrm{m}}^{\mathrm{cal}} \sim$ 4.2 JK^{-1}/mol ($\sim R/2$) at $\mu_0 H <$ 12 T is roughly consistent with classical Monte Carlo results (see the main text).

At $\mu_0 H >$ 12 T, the spin system becomes fully polarized with gapped spin-wave excitations, lifting the degeneracy. The specific heat is then calculated as

$$C_{\mathrm{m}}^{\mathrm{cal}} = \frac{R}{2}(\frac{2}{\sqrt{3}}) \int_{\mathbf{k}\in\mathrm{FBZ}} [\frac{(\frac{\hbar\omega_1}{k_{\mathrm{B}}T})^2 e^{\frac{\hbar\omega_1}{k_{\mathrm{B}}T}}}{(e^{\frac{\hbar\omega_1}{k_{\mathrm{B}}T}}-1)^2} + \frac{(\frac{\hbar\omega_2}{k_{\mathrm{B}}T})^2 e^{\frac{\hbar\omega_2}{k_{\mathrm{B}}T}}}{(e^{\frac{\hbar\omega_2}{k_{\mathrm{B}}T}}-1)^2}]\mathrm{d}\mathbf{k}. \tag{29}$$

The calculated specific heat shows exponential behavior, $C_{\mathrm{m}}^{\mathrm{cal}} \propto \exp(-\Delta/T)$ with $\Delta \sim 1$ K at 13 T (see Supplementary Fig. 18a). As the applied field H increases, the gradient $\nabla_{\mathbf{k}}\omega_1$ around the Γ point in the reciprocal space ($\mathbf{k}$) decreases (see Supplementary Fig. 17a-c), leading to reductions in $v_{\mathrm{m1}}^{\mathrm{cal}}$ (Supplementary Fig. 18b,c).

Supplementary References

[1] Y. Zhao, Z. Ma, Z. He, H. Liao, Y.-C. Wang, J. Wang, and Y. Li, "Quantum annealing of a frustrated magnet," Nat. Commun. **15**, 3495 (2024).

[2] J. R. Olson, "Thermal conductivity of some common cryostat materials between 0.05 and 2 K," Cryogenics **33**, 729 (1993).

[3] X. Hong, M. Gillig, A. R. N. Hanna, S. Chillal, A. T. M. N. Islam, B. Lake, B. Büchner, and C. Hess, "Spinon heat transport in the three-dimensional quantum magnet $PbCuTe_2O_6$," Phys. Rev. Lett. **131**, 256701 (2023).

[4] K. Gofryk, S. Du, C. R. Stanek, J. C. Lashley, X.-Y. Liu, R. K. Schulze, J. L. Smith, D. J. Safarik, D. D. Byler, K. J. McClellan, B. P. Uberuaga, B. L. Scott, and D. A. Andersson, "Anisotropic thermal conductivity in uranium dioxide," Nat. Commun. **5**, 4551 (2014).

[5] X. Hong, M. Gillig, R. Hentrich, W. Yao, V. Kocsis, A. R. Witte, T. Schreiner, D. Baumann, N. Pérez, A. U. B.

Wolter, Y. Li, B. Büchner, and C. Hess, "Strongly scattered phonon heat transport of the candidate Kitaev material $Na_2Co_2TeO_6$," Phys. Rev. B **104**, 144426 (2021).

[6] N. Li, Q. Huang, X. Y. Yue, W. J. Chu, Q. Chen, E. S. Choi, X. Zhao, H. D. Zhou, and X. F. Sun, "Possible itinerant excitations and quantum spin state transitions in the effective spin-1/2 triangular-lattice antiferromagnet $Na_2BaCo(PO_4)_2$," Nat. Commun. **11**, 4216 (2020).

[7] S. Wang, S. Hui, K. Peng, T. P. Bailey, W. Liu, Y. Yan, X. Zhou, X. Tang, and C. Uher, "Low temperature thermoelectric properties of p-type doped single-crystalline SnSe," Appl. Phys. Lett. **112**, 142102 (2018).

[8] E. Zuñiga-Puelles, V. Levytskyi, A. Özden, T. Gürel, N. Bulut, C. Himcinschi, C. Sevik, J. Kortus, and R. Gumeniuk, "Thermoelectric properties and scattering mechanisms in natural PbS," Phys. Rev. B **107**, 195203 (2023).

[9] W. H. Toews, S. S. Zhang, K. A. Ross, H. A. Dabkowska, B. D. Gaulin, and R. W. Hill, "Thermal conductivity of $Ho_2Ti_2O_7$ along the [111] direction," Phys. Rev. Lett. **110**, 217209 (2013).

[10] B. L. Pan, J. M. Ni, L. P. He, Y. J. Yu, Y. Xu, and S. Y. Li, "Specific heat and thermal conductivity of the triangular-lattice rare-earth material $KBaYb(BO_3)_2$ at ultralow temperature," Phys. Rev. B **103**, 104412 (2021).

[11] Y. Shimizu, Y. Kono, T. Sugiyama, S. Kittaka, Y. Shimura, A. Miyake, D. Aoki, and T. Sakakibara, "Development of high-resolution capacitive Faraday magnetometers for sub-Kelvin region," Rev. Sci. Instrum. **92**, 123908 (2021).

[12] Z. Wan, Y. Zhao, X. Chen, Z. Ma, Z. Li, Z. Ouyang, and Y. Li, "Spiral spin liquid in a frustrated honeycomb antiferromagnet: A single-crystal study of GdZnPO," Phys. Rev. Lett. **133**, 236704 (2024).

[13] J. Xiong, Y. Luo, Y. Khoo, S. Jia, R. J. Cava, and N. P. Ong, "High-field Shubnikov–de Haas oscillations in the topological insulator Bi_2Te_2Se," Phys. Rev. B **86**, 045314 (2012).

[14] X Rao, G. Hussain, Q. Huang, W. J. Chu, N. Li, X. Zhao, Z. Dun, E. S. Choi, T. Asaba, L. Chen, L. Li, X. Y. Yue, N. N. Wang, J.-G. Cheng, Y. H. Gao, Y. Shen, J. Zhao, G. Chen, H. D. Zhou, and X. F. Sun, "Survival of itinerant excitations and quantum spin state transitions in $YbMgGaO_4$ with chemical disorder," Nat. Commun. **12**, 4949 (2021).

[15] X. Hong, M. Gillig, W. Yao, L. Janssen, V. Kocsis, S. Gass, Y. Li, A. U. B. Wolter, B. Büchner, and C. Hess, "Phonon thermal transport shaped by strong spin-phonon scattering in a Kitaev material $Na_2Co_2TeO_6$," npj Quantum Mater. **9**, 18 (2024).

[16] B. Y. Pan, Y. Xu, J. M. Ni, S. Y. Zhou, X. C. Hong, X. Qiu, and S. Y. Li, "Unambiguous experimental verification of linear-in-temperature spinon thermal conductivity in an antiferromagnetic Heisenberg chain," Phys. Rev. Lett. **129**, 167201 (2022).

[17] S. Guang, N. Li, R. L. Luo, Q. Huang, Y. Wang, K. Yue, X.and Xia, Q. Li, X. Zhao, G. Chen, H. Zhou, and X. Sun, "Thermal transport of fractionalized antiferromagnetic and field-induced states in the Kitaev material $Na_2Co_2TeO_6$," Phys. Rev. B **107**, 184423 (2023).

[18] K. Fujiwara, S. Kitamura, and T. Morimoto, "Thermal Hall responses in frustrated honeycomb spin systems," Phys. Rev. B **106**, 035113 (2022).

[19] H. Zhang, C. Xu, C. Carnahan, M. Sretenovic, N. Suri, D. Xiao, and X. Ke, "Anomalous thermal Hall effect in an insulating van der Waals magnet," Phys. Rev. Lett. **127**, 247202 (2021).

[20] P. Czajka, T. Gao, M. Hirschberger, P. Lampen-Kelley, A. Banerjee, N. Quirk, D. G. Mandrus, S. E. Nagler, and N. P. Ong, “Planar thermal Hall effect of topological bosons in the Kitaev magnet α-$RuCl_3$,” Nat. Mater. **22**, 36 (2023).

[21] X. Li, B. Fauqué, Z. Zhu, and K. Behnia, “Phonon thermal Hall effect in strontium titanate,” Phys. Rev. Lett. **124**, 105901 (2020).

[22] D. Zhang, K.-W. Chen, G. Zheng, F. Yu, M. Shi, Y. Zhu, A. Chan, K. Jenkins, J. Ying, Z. Xiang, X. Chen, and L. Li, “Large oscillatory thermal hall effect in kagome metals,” Nat. Commun. **15**, 6224 (2024).

[23] J. Liu, L. Yuan, X. Li, B. Li, K. Zhao, H. Liao, and Y. Li, “Gapless spin liquid behavior in a kagome Heisenberg antiferromagnet with randomly distributed hexagons of alternate bonds,” Phys. Rev. B **105**, 024418 (2022).

[24] J. Liu, B. Liu, L. Yuan, B. Li, L. Xie, X. Chen, H. Zhang, D. Xu, W. Tong, J. Wang, and Y. Li, “Frustrated magnetism of the triangular-lattice antiferromagnets α-CrOOH and α-CrOOD,” New J. Phys. **23**, 033040 (2021).

[25] S. Toth and B. Lake, “Linear spin wave theory for single-Q incommensurate magnetic structures,” J. Phys.: Condens. Matter **27**, 166002 (2015).